# Sustainable ammonia synthesis via thermochemical reaction cycle

by

Michael Gregory Heidlage

B.S., University of Missouri, 2012

AN ABSTRACT OF A DISSERTATION

submitted in partial fulfillment of the requirements for the degree

DOCTOR OF PHILOSOPHY

Department of Chemical Engineering
College of Engineering

KANSAS STATE UNIVERSITY
Manhattan, Kansas

2018

# Abstract

Since its inception, the Haber-Bosch (HB) process for ammonia ($NH_3$) synthesis has allowed for a significant increase in global food production as well as a simultaneous decrease in global hunger and malnutrition. The HB process is estimated to be responsible for the subsistence of 40% of the world population as approximately 85% of the over 182 metric tons of $NH_3$ produced in 2017 was used as fertilizer for crop production. The natural gas consumed (mostly to generate $H_2$) represents approximately 2% of the global energy budget, while the $CO_2$ produced is about 2.5% of all global fossil $CO_2$ emissions. Approximately 40% of food consumed is essentially natural gas transformed by the HB process into agricultural products. However global food production will need to double due to expected increase in world population to 9.6 billion by 2050 and rising demand for protein among developing nations.

A novel thermochemical reaction cycle for sustainable $NH_3$ synthesis at atmospheric pressure is explored herein. Both thermochemical and kinetic rationales are discussed regarding choice of Mn as the cycled reactant. The energetic driving force for these reactions is conceptually derived from concentrated solar energy.

Mn was reacted with $N_2$ forming Mn-nitride, corrosion of Mn-nitride with steam at 500 °C formed MnO and $NH_3$, and lastly MnO was reduced at 1150 °C in a 4 vol % $CH_4$ – 96 vol % $N_2$ stream to Mn-nitride closing the cycle. Optimum nitridation at 800 °C and 120 min produced a $Mn_6N_{2.58}$-rich Mn-nitride mixture containing 8.7 ± 0.9 wt. % nitrogen. $NH_3$ yield was limited to 0.04 after 120 min during nitride corrosion but addition of a NaOH promotor improved $NH_3$ yield to 0.54. $Mn_6N_{2.58}$ yield was 0.381 ± 0.083 after MnO reduction for 30 min with CO and $H_2$ but no $CO_2$ detected in the product.

Mn-nitridation kinetics were investigated at temperatures between 600 and 800 °C for 10 and 44 μm reactant powder particle sizes. That equilibrium conversion decreased with increasing temperature was confirmed. Jander's rate law, which assumes gaseous reactant diffusion through a solid product layer, described the experimental data reasonably well. The rate constants and initial rates were as much as an order of magnitude greater for the 10 μm Mn reactant particle size. Additionally the activation energy was found to be 44.1 kJ $mol^{-1}$ less for the 10 μm reactant particle size. Reducing the particle size had a small but positive effect on Mn-nitridation kinetics. Further reducing particle size will likely have a greater impact.

A review of relevant classical thermodynamics is discussed with special attention paid to open systems. Confidence issues regarding over-reliance on x-ray diffraction are considered with options suggested for mitigation. Opportunities for future work are assessed.

# Sustainable ammonia synthesis via thermochemical reaction cycle

by

Michael Gregory Heidlage

B.S., University of Missouri, 2012

A DISSERTATION

submitted in partial fulfillment of the requirements for the degree

DOCTOR OF PHILOSOPHY

Department of Chemical Engineering
College of Engineering

KANSAS STATE UNIVERSITY
Manhattan, Kansas

2018

Approved by:

Major Professor
Dr. Peter H. Pfromm

# Copyright

© Michael G. Heidlage 2018.

# Abstract

Since its inception, the Haber-Bosch (HB) process for ammonia ($NH_3$) synthesis has allowed for a significant increase in global food production as well as a simultaneous decrease in global hunger and malnutrition. The HB process is estimated to be responsible for the subsistence of 40% of the world population as approximately 85% of the over 182 metric tons of $NH_3$ produced in 2017 was used as fertilizer for crop production. The natural gas consumed (mostly to generate $H_2$) represents approximately 2% of the global energy budget, while the $CO_2$ produced is about 2.5% of all global fossil $CO_2$ emissions. Approximately 40% of food consumed is essentially natural gas transformed by the HB process into agricultural products. However global food production will need to double due to expected increase in world population to 9.6 billion by 2050 and rising demand for protein among developing nations.

A novel thermochemical reaction cycle for sustainable $NH_3$ synthesis at atmospheric pressure is explored herein. Both thermochemical and kinetic rationales are discussed regarding choice of Mn as the cycled reactant. The energetic driving force for these reactions is conceptually derived from concentrated solar energy.

Mn was reacted with $N_2$ forming Mn-nitride, corrosion of Mn-nitride with steam at 500 °C formed MnO and $NH_3$, and lastly MnO was reduced at 1150 °C in a 4 vol % $CH_4$ – 96 vol % $N_2$ stream to Mn-nitride closing the cycle. Optimum nitridation at 800 °C and 120 min produced a $Mn_6N_{2.58}$-rich Mn-nitride mixture containing 8.7 ± 0.9 wt. % nitrogen. $NH_3$ yield was limited to 0.04 after 120 min during nitride corrosion but addition of a NaOH promotor improved $NH_3$ yield to 0.54. $Mn_6N_{2.58}$ yield was 0.381 ± 0.083 after MnO reduction for 30 min with CO and $H_2$ but no $CO_2$ detected in the product.

Mn-nitridation kinetics were investigated at temperatures between 600 and 800 °C for 10 and 44 μm reactant powder particle sizes. That equilibrium conversion decreased with increasing temperature was confirmed. Jander's rate law, which assumes gaseous reactant diffusion through a solid product layer, described the experimental data reasonably well. The rate constants and initial rates were as much as an order of magnitude greater for the 10 μm Mn reactant particle size. Additionally the activation energy was found to be 44.1 kJ $mol^{-1}$ less for the 10 μm reactant particle size. Reducing the particle size had a small but positive effect on Mn-nitridation kinetics. Further reducing particle size will likely have a greater impact.

A review of relevant classical thermodynamics is discussed with special attention paid to open systems. Confidence issues regarding over-reliance on x-ray diffraction are considered with options suggested for mitigation. Opportunities for future work are assessed.

# Table of Contents

# List of Figures

# List of Tables

# Acknowledgements

I would first like to thank my major advisor Dr. Peter Pfromm and co-advisor Dr. Mary Rezac for their endless patience and sage advice. Their encouragement and guidance always served to improve my skills and increase my knowledge as a researcher. In the process, they have become both personal and professional role models for me. I am exceptionally grateful.

I also wish to thank the current and former Pfromm-Rezac group members for their friendship, support, and advice. I specifically want to thank Matthew Young, Michael Wales, Leslie Schulte, John Stanford, Yixiao Li, and Jared Carson. I will miss the late nights in the lab. I also wish to thank Ronald Michalsky who provided significant advice and guidance regarding the direction of the research.

I sincerely appreciate my PhD supervisory committee members. From job search and career advice to gathering SEM images in the lab, Dr. Gurpreet Singh always made time for me. Dr. Donghai Wang was consistently encouraging and frequently offered his analytical instrumentation to the service of this research. I am truly thankful to both.

Special thanks to Kansas State University's senior scientific glassblower James Hodgson for his technical assistance, process design ideas, and his friendship. This research would be less developed without his input. Technical assistance provided by Dave Threewit is also greatly appreciated.

I have had the pleasure of working with several undergraduate research assistants: Kyle Snow, Elizabeth Kezar, Bradley Peterson, Gary Roberts III, and Brady Rinaldi. They each brought their own brand of enthusiasm and determination to the research and I appreciate their contributions.

Also thank you to the staff members of the Department of Chemical Engineering: Florence Sperman, Pat Nelson, Karey DeBardeleben, Danita Deters and Debi Wahl. I especially thank Karen Strathman for her work ethic, know-how, and perpetual patience.

This material is based upon work supported by National Science Foundation Grant: From Crops to Commuting: Integrating the Social, Technological, and Agricultural Aspects of Renewable and Sustainable Biorefining (I-STAR); NSF Award No.: DGE-0903701.

This work was supported by the U.S. Department of Energy, Office of Science, Basic Energy Sciences, under Award # DE-SC0016453.

Additional funding was provided by the National Institute of Food and Agriculture, U.S. Department of Agriculture, under Agreement No. 2011-67009-20055.

# Dedication

To Maria, Alissa, Erica, Mom, Dad, David and Nathan for their love, support, energy and optimism.

# Chapter 1 - Introduction

## 1.1 Motivation

Nitrogen is the most common yield-limiting nutrient in agriculture[1] even though nitrogen gas (dinitrogen, $N_2$) comprises approximately 80% of Earth's atmosphere.[2] This dichotomy stems from the large bond dissociation enthalpy of $N_2$ (945 kJ $mol^{-1}$)[3] which renders it unusable by most biological systems.[4] Fixed nitrogen (as an agricultural input) is produced by first cleaving the $N_2$ triple bond then attaching the N-atoms to hydrogen ($NH_3$ or $NH_4^+$) or oxygen ($NO_2$). This process can occur naturally or synthetically and is known generally as "nitrogen fixation".[2] Today, natural nitrogen fixation processes provide about half of the nitrogen required to sustain the global population while the other half is provided by inorganic fertilizers such as ammonia ($NH_3$) produced industrially via the Haber-Bosch (HB) process.[1]

Synthetic $NH_3$ from the HB process is partially credited as "the fuel" which propelled the substantial increase in food production known as the "green revolution" of the 20$^{th}$ century.[5,6] Since its inception, the HB process for $NH_3$ synthesis has allowed for a significant increase in global food production as well as a simultaneous decrease in global hunger and malnutrition.[7] Fritz Haber successfully demonstrated the chemistry at the lab-scale in 1909,[1] a discovery that earned him the Nobel Prize in chemistry in 1918.[8] Carl Bosch won a Nobel Prize in Chemistry in 1931 for developing the chemical high pressure methods necessary for industrial scale $NH_3$ production.[9] Industrial-scale $NH_3$ synthesis began in 1913, a mere 4 years after Haber's initial discovery,[1] producing 30 metric tons (t) $day^{-1}$ at 130 atm.[7] Today over 80% of the nitrogen found in human tissues, on average, originates from ammonia synthesized from the Haber-Bosch process.[10] Figure 1.1 shows the global human population over time[11,12] superimposed on the global consumption of synthetic nitrogen fertilizers[4,6,13]. Notice both curves have similar inflection points

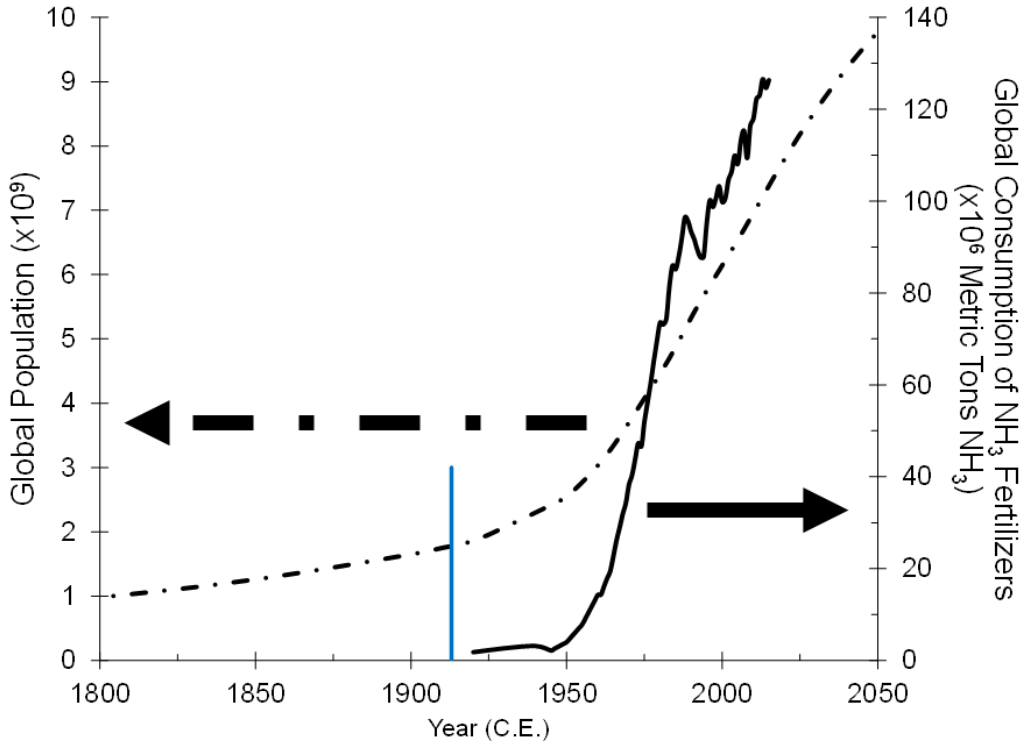


**Figure 1.1: The correlation between human population growth (dashed) and availability of fixed nitrogen available for fertilizer (solid). The vertical blue line at year 1913 represents the first industrial scale $NH_3$ facility, included as a reference.**

suggesting industrial inorganic $NH_3$ synthesis is at least partially responsible for the population growth rate. It is now estimated that the fixed nitrogen provided by the HB process is responsible for the subsistence of 40% of the global population.[6]

## 1.2 Modern Industrial Ammonia Synthesis

Approximately 85%[14] of the over 182 t $NH_3$ produced globally per year is consumed as fertilizer.[15] Other uses for ammonia include explosives, plastics, synthetic resins and fibers, as well as feedstocks for other chemicals.[15] However, global food production will need to double due to the expected increase in world population to over 9.7 billion[11] by 2050 and rising demand for protein among developing nations.[16]

Figure 1.2 shows a simplified overview of the HB process.[17] The steam reforming block converts natural gas (primarily methane, $CH_4$) into the $H_2$ reactant necessary for catalytic $NH_3$

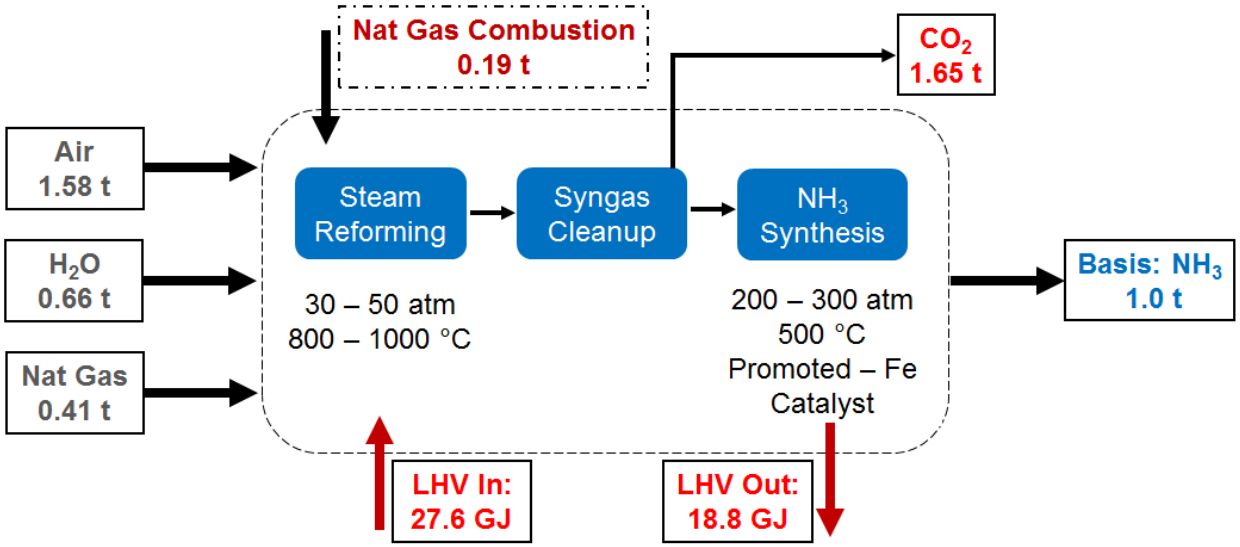


**Figure 1.2: Simplified overview of industrial $NH_3$ synthesis via the HB process. Basis taken as 1.0 t $NH_3$ output.**

synthesis.[18] The syngas cleanup block removes the impurities from the reformer effluent stream, preparing the reactant $H_2$ and $N_2$ gases for catalytic $NH_3$ synthesis.[19] The $NH_3$ synthesis step converts $N_2$ and $H_2$, supplied in a 1:3 ratio,[20] into $NH_3$ at pressures between 180 – 300 atm and temperatures of approximately 500 °C.[21]

Advantages of the HB process revolve around its maturity. Consequently, further efficiency improvements of modern HB plants will be incremental as total energy use of 28 GJ $t^{-1}$ $NH_3$[22] is quite close to the thermodynamic minimum of 20.9 GJ $t^{-1}$ $NH_3$.[23]

The disadvantages of industrial $NH_3$ production via HB concern its long term sustainability and technical restrictions. The HB process consumes approximately 0.6 t natural gas as both a source of hydrogen and combustion energy and emits 1.6 t $CO_2$ $t^{-1}$ $NH_3$, specifically coupling food production with fossil fuel consumption and greenhouse gas emissions.[18,21] The natural gas consumed represents 2-3% of the global energy budget,[24] and the $CO_2$ produced is approximately 2.5% of all global fossil $CO_2$ emissions.[25] One may infer that approximately 40% of food consumed is in effect natural gas transformed by the HB process into agricultural products.

The extreme operating conditions (Figure 1.2), make the HB process one of the more technically demanding in the chemical industry. Large economies of scale are required for profitability as well as a large uninterrupted supply of natural gas as the $H_2$ source. In turn, the process complexity and scale of investment limits possible locations to politically stable and technically advanced regions. HB plants producing 1000 t $NH_3$ $day^{-1}$ were built in the late 1960's[26] while newer plants have capacities of at least 1500 t $NH_3$ $day^{-1}$.[27] A modern HB $NH_3$ synthesis plant costs approximately $300 million in capital costs for a capacity of 2000 t $NH_3$ $day^{-1}$.[26]

These large operating pressures are the result of the unfavorable gas-phase thermodynamic equilibrium reaction shown in eq (1)[19].

$$\frac{1}{2}N_2 + \frac{3}{2}H_2 \xleftrightarrow{\text{Promoted-Fe}} NH_3;\ \Delta H°_{25°C} = -45.9\ kJ\ mol^{-1} \quad (1)$$

According to Le Chatelier's principle, equilibrium will favor the products as pressure increases.[28] However, even at 300 atm, $NH_3$ yield is still less than 25% per pass.[20] Thus condensing and separating the $NH_3$ and recycling the unreacted $N_2$–$H_2$ mixture is required. Between 4 and 6 kg of reactant gas mixture are recycled (not shown in Figure 1.2) per kg of $NH_3$ synthesized.[20] Only the fortuitously simple separation of easily condensable ammonia from unreacted synthesis gas renders the process viable at all.

The primary opportunities for HB efficiency improvements focus on $H_2$ generation instead of $NH_3$ synthesis. In fact, the $NH_3$ synthesis block and especially the catalyst itself have been the subject of significant study since the beginning,[29,30] and are widely considered to be optimized already[31]. Meanwhile, roughly 84% of the energy necessary for the HB process is consumed by the production of the $H_2$ feedstock while 16% is used for compression work.[22] Additionally, about 66% of $CO_2$ emissions derive from the $H_2$ generation stage.[32]

## 1.3 Alternatives to Modern Industrial Ammonia Synthesis

The maturity of the HB process for industrial $NH_3$ synthesis provides a significant barrier to new $NH_3$ production technologies. Several alternatives to industrial HB $NH_3$ synthesis have received significant attention but have not yet reached fruition. Electrochemical $NH_3$ syntheses[33-37] typically require novel electrolytes,[38] or have low $NH_3$ yields due to poor electrode conductivity[39]. An additional drawback stems from the current fossil fuel electricity sources required to transfer 3 electrons per $NH_3$ molecule formed (assuming the cell current efficiency is perfect). Advancing this technology past the laboratory stage will require significant improvement in the catalyst and electrolyte and little economic analysis has been performed.[40] $NH_3$ synthesis methods which emulate enzymatic catalysts via transition metal coordination complexes feature significantly higher yields but often require a sacrificial and expensive reducing equivalent.[41-44] Another option is improve the HB process by replacing the steam reforming of natural gas with a bolt-on renewable $H_2$ generation method such as electrolysis[17] or solar thermochemical water splitting[45].

## 1.4 Cyclical Thermochemical Ammonia Synthesis

The work proposed here attempts to break the decades-old model of food production from fossil fuel consumption via industrial ammonia fertilizer synthesis. In lieu of the "simultaneous" $NH_3$ synthesis step of the HB process, an alternative strategy for $NH_3$ formation in which the dinitrogen cleavage and protonation steps are separated into separate chemical reactions is explored here. One iteration of the process is shown in Figure 1.3. Here step 1 consists of a reaction between a transition metal nitride, manufactured according to eq (2), and steam to produce ammonia and a transition metal oxide as shown in eq (3) using generic stoichiometry.

$$\frac{a}{b}M + \frac{1}{2}N_2 \leftrightarrow \frac{1}{b}M_aN_b \quad (2)$$

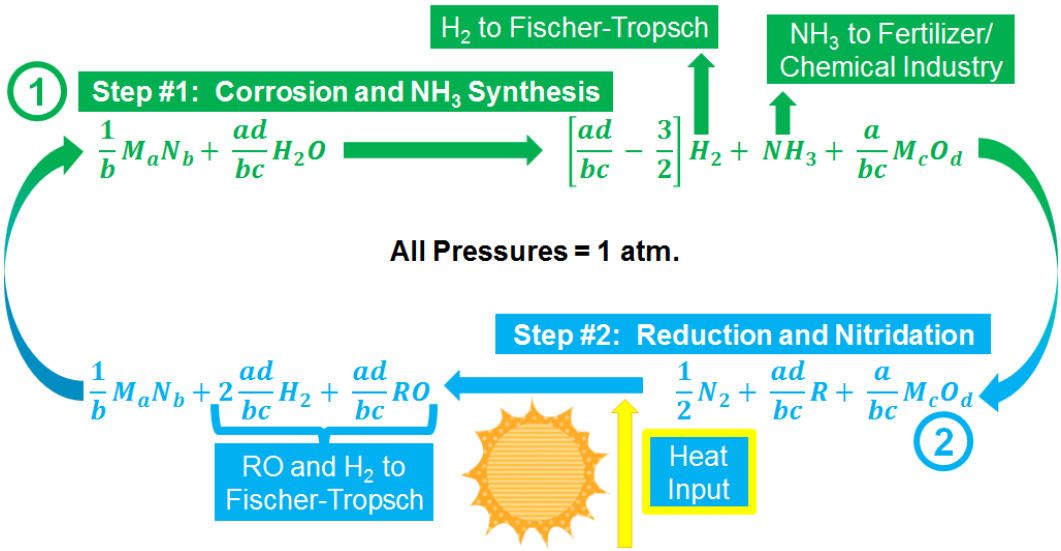


**Figure 1.3: Schematic of a chemical loop for the $NH_3$ thermochemical cycle. Step 1: A metal nitride reacts with steam to form $NH_3$, a metal oxide, and $H_2$, corresponds with eq (3). Step 2: The metal oxide is reduced at elevated temperature in a dilute reducing agent R/$N_2$ stream to form syngas (CO and $H_2$ if R is $CH_4$) and reproduce the nitride. Combines eqs (2) and (4).**

$$\frac{1}{b}M_aN_b + \frac{ad}{bc}H_2O \leftrightarrow \left[\frac{ad}{bc} - \frac{3}{2}\right]H_2 + NH_3 + \frac{a}{bc}M_cO_d \quad (3)$$

Step 2 of Figure 1.3 reduces the oxide produced in step one using a reducing agent (such as solid carbon or $CH_4$), denoted as R in eq (4), diluted in an $N_2$ gas stream to recover the metal nitride.

$$\frac{a}{bc}M_cO_d + \frac{ad}{bc}R \leftrightarrow \frac{a}{b}M + \frac{ad}{bc}RO \quad (4)$$

Ideally the energy input necessary for the endothermic reduction step would come from a renewable source such as concentrated solar power. Direct solar use provides the energetic driving force for the reduction reaction as heat, mitigating the inefficiencies which accompany conversion to electrical work as in photovoltaic systems. Accordingly, the solar thermochemical $NH_3$ synthesis cycle can be considered a means to chemically store renewable solar energy. The use of stable reaction products based on inexpensive raw materials rather than sensitive and sophisticated catalytic materials allows for robust shutdown/startup that is required due to intermittent insolation.

That $H_2$ is generated either directly from steam or electrolytically rather than from natural gas is paramount to the potentially greater sustainability of the solar thermochemical $NH_3$ cycle over the HB process. However, using $CH_4$ (the primary component of natural gas) as the reducing agent, R in eq (4) and Figure 1.3, yields syngas (CO and $H_2$) which is a net energy upgrade alone over the natural gas consumed by the process.[46] Additionally, each reaction (dinitrogen cleavage, protonation) can be optimized individually instead of balancing the competing requirements of each as is necessary in typical HB heterogeneous catalysis.[47] The process conditions, more mild than the Haber-Bosch process, may allow for economically viable smaller ammonia production facilities with reduced capital cost to operate closer to the end user. This is vital to encourage fertilizer production in many developing countries, where the majority of under-utilized arable land exists,[48] in order to double crop production by 2050[16]. Ideally the proposed cycle could be incorporated into a process small enough to be operated by a single farmer.

## 1.5 Small-Scale Ammonia Synthesis

Despite the aforementioned drawbacks, the HB process remains the most efficient and economically viable means to industrially produce the fixed nitrogen necessary to sustain the global population. Indeed the significant investment in novel nitrogen fixation methods over the last century[49-51] has failed at dethroning HB from its status as industrial juggernaut. Instead, new routes to $NH_3$ should focus on down-scalable processes in those regions where HB is less profitable.[17]

Today a new HB $NH_3$ plant requires approximately $300 million in capital investment to produce 2000 t $NH_3$ $day^{-1}$.[26] These large facilities and capital costs limit HB to politically stable regions with a technically advanced workforce.[27] However, it is the developing regions where the majority of the under-utilized arable exists on the planet.[48] Future proposals for $NH_3$ greenfield

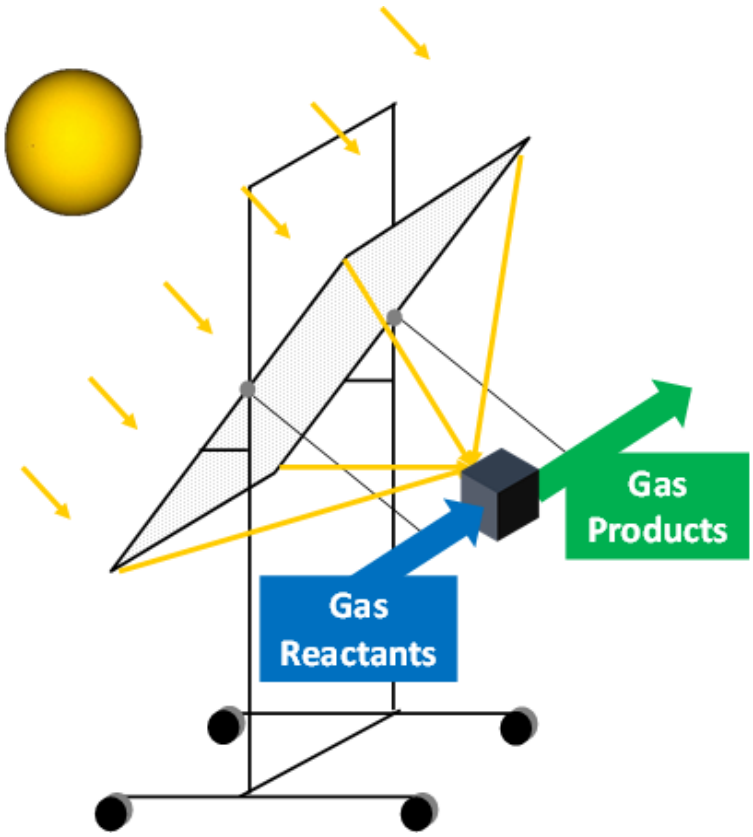


**Figure 1.4: A simplified schematic of the solar concentrator for $NH_3$ synthesis deployed at Kansas State University. Gases are cycled over a solid reactant. The entire system stands approx. 2 m tall and the Fresnel lens has an area of about 1 $m^2$. It can be operated by a single user.**

processes should target this niche as abundant HB plants present significant economic barriers to well-established $NH_3$ markets.[17]

Instead operation near atmospheric pressure and accommodation of intermittent renewable energy form the foundation for $NH_3$ production at a much smaller scale while requiring significantly less capital investment and allowing operation much closer to the end-user. A simplified schematic of the solar concentrator for $NH_3$ synthesis deployed at Kansas State University[52] is provided in Figure 1.4. This process may serve to reduce the economic barriers into less-established $NH_3$ markets by potentially accommodating more frequent disruptions as workforce competency, political stability, and transportation infrastructure are less relevant.

# Chapter 2 - Thermochemical Synthesis of Ammonia and Syngas from Natural Gas at Atmospheric Pressure

## 2.1 Abstract

Ammonia is a vital agricultural input and could be a carbon-free energy vector. An experimental proof-of-concept of a novel thermochemical cycle to produce $NH_3$ and syngas ($CO$-$H_2$) at atmospheric pressure from $N_2$, steam, and shale gas ($CH_4$) is demonstrated here: Mn was reacted with $N_2$ forming Mn-nitride, corrosion of Mn-nitride with steam at 500 °C formed MnO and $NH_3$, and lastly MnO was reduced at 1150 °C in a 4 vol % $CH_4$ – 96 vol % $N_2$ stream to Mn-nitride closing the cycle. Optimum nitridation at 800 °C and 120 min produced a $Mn_6N_{2.58}$-rich Mn-nitride mixture containing 8.7 ± 0.9 wt. % nitrogen. $NH_3$ yield was limited to 0.04 after 120 min during nitride corrosion but addition of a NaOH promotor improved $NH_3$ yield to 0.54. $Mn_6N_{2.58}$ yield was 0.381 ± 0.083 after MnO reduction for 30 min with CO and $H_2$ but no $CO_2$ detected in the product.

## 2.2 Introduction

About 85% of the annual 176 million metric tons (t) of ammonia ($NH_3$) produced globally is consumed as fertilizer for crop production.[19,53] However global food production will need to double by 2050 to accommodate the expected increase in world population to over 9 billion and the rising demand for protein among developing nations.[16] In turn, $NH_3$ production will need to increase to accommodate the expected fertilizer demand required for additional high-yield crop production.[4,53]

The Haber-Bosch (H.-B.) process, since its inception in the early twentieth century, has driven a significant increase in global food production and decrease in hunger and malnutrition via

*Reprinted (adapted) with permission from Heidlage, M. G.; Kezar, E. A.; Snow, K. C.; Pfromm, P. H. Thermochemical Synthesis of Ammonia and Syngas from Natural Gas at Atmospheric Pressure. *Ind. Eng. Chem. Res.* **2017***, 56*, 14014-14024. Copyright 2017 American Chemical Society.

synthesis of $NH_3$ from air and water.[7] However significant energy input is required as atmospheric nitrogen fixation to $NH_3$ is difficult due to the strong triple bond, nonpolar nature, and large ionization potential of $N_2$.[54] 4-6 kg of the $N_2$-$H_2$ reactant mixture is recycled per kg $NH_3$ produced with a maximum $NH_3$ yield of 25% per pass despite temperatures between 400-600 °C, the requisite catalyst, and pressures up to 300 bar which drive chemical equilibrium towards $NH_3$ and increase the reaction rate.[18,20,55] The severe operating conditions require significant capital investment and the associated economies of scale demand large facilities producing on the order of 1000-1500 t $NH_3$ $day^{-1}$ or more.[22] The process consumes about 2% of the global energy budget,[24] approximately 28-40 GJ $t^{-1}$ $NH_3$ in North America,[20,22] as natural gas for both combustion and $H_2$ generation by steam reforming. Accordingly the H.-B. process emits about 2.3 t $CO_2$ $t^{-1}$ $NH_3$ produced under the best conditions,[22] explicitly linking food production to fossil $CO_2$ emissions by $NH_3$-based fertilizers.

Alternative methods at the laboratory stage for $NH_3$ production at mild conditions include electrochemical $NH_3$ synthesis[36,38,39,56] and liquid-phase synthesis via transition metal coordination complexes[54,57]. Electrochemical methods require novel electrolytes,[38] or have low $NH_3$ yields due to poor conductivity,[39] and require 3 electrons per $NH_3$ molecule formed. Approaches utilizing coordination complexes have higher yields but typically require a complex and costly external reducing equivalent to generate the dinitrogen complex.[41,43]

Inorganic avenues to $NH_3$ synthesis have been the subject of investigation for over a century.[49-51] The H.-B. catalysts simultaneously activate dinitrogen by splitting the N-N triple bond, and enable the reaction of $N_2$ with $H_2$ to form $NH_3$. A different approach would be to first activate dinitrogen, and have it react with $H_2$ in a separate step to harvest $NH_3$. Haber and co-

workers tested inorganic nitrides for nitrogen activation early on, but discarded the approach since their target was conversion of a $H_2$ and $N_2$ mixture to $NH_3$ over a solid contact in one step.[58]

Recently, a two-step solar thermochemical cycle for $NH_3$ synthesis at atmospheric pressure was proposed.[59-62] The cycle begins with endothermic carbothermal reduction of $Al_2O_3$ under $N_2$ to produce CO and aluminum nitride (AlN) at temperatures of 1750-2000 °C.[62] The AlN subsequently undergoes exothermic hydrolysis at temperatures of 900-1200 °C which produces the desired $NH_3$ and recovers the $Al_2O_3$ to close the cycle.[59-61] The net products, CO and $NH_3$, store intermittent solar energy as valuable fuels and chemicals.[63-65] However, the temperatures required for the endothermic reduction reaction would necessitate exotic and expensive materials for large scale industrial reactors.[63-65]

Another solar thermochemical cycle has been demonstrated using a Fresnel-lens focusing solar radiation on Cr, instead of Al, as the cycled reactant.[52] Cr was reacted with $N_2$ at approximately 1000 °C to produce $Cr_2N$ (85% after 5.6 min) which converted to cubic CrN with time. The nitride then underwent corrosion with steam at 1000 °C which formed $Cr_2O_3$ and CrO. However, this reaction was characterized by low $NH_3$ yields liberating only 0.15 mol % of the lattice nitrogen to form $NH_3$.[52] The cycle was closed by reducing $Cr_2O_3$ at 1000-1600 °C under CO and $H_2$ to reproduce Cr. CO and $H_2$ were conceptually to be derived from renewable biomass. The molar yield near the surface of the particles was found to be approximately 83%, however diffusion in the solid particles (diameter about 44μm) quickly limited further conversion to $NH_3$.[52]

An immediate technical challenge in the development of a thermochemical cycle for $NH_3$ synthesis is the creation of a cycled reactant which can undergo the successive nitridation, corrosion, and reduction reactions with acceptable yields and kinetics at temperatures appropriate for industrial solar equipment.[47,66] Combining two desired properties into a single composite

reactant material made from two elements has been successful in Li-air batteries,[67] solar thermochemical $H_2O$ and $CO_2$ splitting,[68-70] and catalysts for $NH_3$ synthesis[30]. Thermodynamic trends have shown the majority of individual elements either favor carbothermal reduction or nitridation and $NH_3$ liberation but not all 3 reactions.[66] The 3 elements (V, Ga, and Mo) identified as thermodynamically favored for all 3 reactions are unattractive as the elements or the corresponding oxides or nitrides exhibit poor kinetics or phase changes at operating temperatures.[66] Addition of CaO or $Ca(OH)_2$ to Cr-nitride was thought to assist in protonation of N to $NH_3$ however this only increased $NH_3$ yield 1.56-fold over Cr-nitride alone.[52] The modest increase in $NH_3$ yield indicates $NH_3$ formation is limited by diffusion or low $N^{3-}$ concentrations in the nitride.[52] Furthermore, additional thermodynamic analysis indicates that the choice of metal reactant will either favor enthalpy transfer between the exothermic $NH_3$ synthesis reaction and the endothermic oxide reduction step, or the reactant will require less chemical reducing agent during oxide reduction, but not both.[47]

## 2.3 Theory

A reaction cycle involving three thermochemical reactions in two process steps (Figure 2.1) is explored here. The reaction enthalpies ($\Delta H_{rxn}$, kJ $mol^{-1}$) and Gibbs free energies ($\Delta G_{rxn}$, kJ $mol^{-1}$) in eqs (5-(8) at the temperatures indicated are calculated from the limited literature data available.[71,72] The first step, exothermally produces $Mn_5N_2$ from Mn and gaseous $N_2$ (eq (5)). The second exothermic step is the corrosion of the nitride with steam producing $NH_3$ and MnO (eq (6)). The endothermic third and final step reduces MnO with $CH_4$ producing CO, $H_2$, and Mn to close the cycle (eq (7)). The overall proposed cycle consumes energy overall as shown in eq (8). An energy source is required at the endothermic reduction step, eq (7), which absorbs energy at a higher temperature than the exothermic nitridation, eq (5), and $NH_3$ synthesis, eq (6), steps release

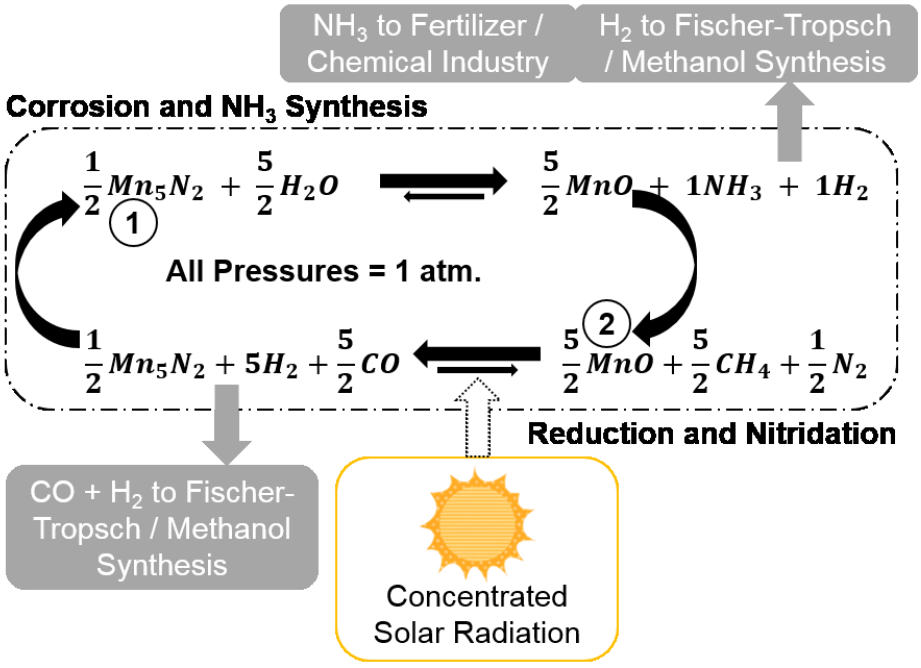


**Figure 2.1: Conceptual scheme for $NH_3$ and syngas (CO and $H_2$) production via a solar thermochemical reaction cycle at atmospheric pressure. $Mn_5N_2$ undergoes corrosion with steam in step 1 to produce $NH_3$ and MnO. The latter is recycled in step 2 via reduction with $CH_4$ diluted by $N_2$ to produce syngas and reproduce $Mn_5N_2$ for reuse in step 1.**

it. This energy could be supplied from renewable electricity, solar thermal energy, or even by combustion of the produced syngas.

Choice of Mn as the cycled reactant explored here arose from the thermochemistry of the individual reactions, eqs (5-(7) of the $NH_3$ synthesis cycle. The Gibbs free energies indicate that each reaction proceeds spontaneously toward the products at the specified temperatures. Gibbs free energy mapping, considering carbothermal oxide reduction of numerous elements, showed that few elements will exhibit an $NH_3$ synthesis cycle in which all reactions proceed spontaneously at realistic process temperatures.[66] Fortunately the thermochemistry improves when methanothermal reduction, eq (7), is considered in place of carbothermal reduction and Mn is the cycled reactant (see Gibbs reaction energies of eqs (5-(7)).

$$\frac{5}{2}Mn_{(s)} + \frac{1}{2}N_{2(g)} \leftrightarrow \frac{1}{2}Mn_5N_{2(s)} \quad (5)$$

$$\Delta H_{Rxn1}^{T=800°C} = -91.0\ kJ\ mol^{-1} \qquad \Delta G_{Rxn1}^{T=800°C} = -64.3\ kJ\ mol^{-1}$$

$$\frac{1}{2}Mn_5N_{2(s)} + \frac{5}{2}H_2O_{(g)} \leftrightarrow \frac{5}{2}MnO_{(s)} + NH_{3(g)} + H_{2(g)} \quad (6)$$

$$\Delta H_{Rxn2}^{T=500°C} = -302.4\ kJ\ mol^{-1} \qquad \Delta G_{Rxn2}^{T=500°C} = -230.5\ kJ\ mol^{-1}$$

$$\frac{5}{2}MnO_{(s)} + \frac{5}{2}CH_{4(g)} \leftrightarrow \frac{5}{2}Mn_{(s)} + \frac{5}{2}CO_{(g)} + 5H_{2(g)} \quad (7)$$

$$\Delta H_{Rxn3}^{T=1150°C} = 916\ kJ\ mol^{-1} \qquad \Delta G_{Rxn3}^{T=1150°C} = -57.1\ kJ\ mol^{-1}$$

$$\frac{1}{2}N_{2(g)} + \frac{5}{2}H_2O_{(g)} + \frac{5}{2}CH_{4(g)} \leftrightarrow NH_{3(g)} + \frac{5}{2}CO_{(g)} + 6H_{2(g)} \quad (8)$$

$$\Delta H_{Overall}^{T=25°C} = 469.3\ kJ\ mol^{-1}$$

Rigorous thermodynamic analysis is inhibited by the lack of quality thermochemical data available for Mn-nitrides. Published thermochemical data appears to be available for only 2 Mn-nitride compounds, $Mn_4N$ and $Mn_5N_2$, up to 527 °C and must be extrapolated for the work described here.[72] $Mn_5N_2$ was chosen for thermochemical calculations as the higher N/Mn ratio suggests potential for greater $NH_3$ production per mass of Mn.

A simple analysis of solar and chemical energy inputs and outputs is provided in Figure 2.2. Here an idealized and completely reversible process is assumed. Chemical energies are represented using their lower heating values (LHV).[73] The syngas coproduct (4.1 t CO $t^{-1}$ $NH_3$ and 0.7 t $H_2$ $t^{-1}$ $NH_3$) of the solar thermochemical $NH_3$ cycle contains more energy (9.1 GJ $t^{-1}$ $NH_3$) than is provided by natural gas input (2.4 t $CH_4$ $t^{-1}$ $NH_3$). The solar energy input is based on the enthalpy required for the endothermic reduction reaction (ΔH, eq (7)) scaled for production of 1 t $NH_3$ taken as the basis.

The natural gas required as a chemical reducing agent supplies 117.6 GJ $t^{-1}$ $NH_3$ however 126.7 GJ $t^{-1}$ $NH_3$ is produced as syngas in addition to the 18.6 GJ of the $NH_3$ itself according to Figure 2.2. The energy upgrade of the syngas coproduct relative to the natural gas input is a benefit of the solar process compared to the H.-B. process which converts natural gas into $CO_2$.[19] The

solar process can be considered to store intermittent solar radiation in the form of syngas and $NH_3$ products.

Figure 2.2 is based on an ideal process with several simplifying assumptions. The energy requirements to run the process such as $N_2$ separation from air, input gas conditioning, and exit gas separation are neglected. These energies are negligible when compared to the energy required for the endothermic reduction step.[17] Energy produced in the exothermic reactions, eqs (5 and (6) is neglected as the lower reaction temperatures relative to eq (7) limit heat integration. This neglected excess process heat may be used to partially compensate for the energy requirements mentioned earlier or converted to electricity.[27]

Benefits of $NH_3$ production via the proposed cycle over the conventional H.-B. process include: (1) conversion of natural gas ($CH_4$) to valuable syngas, a potential feedstock for methanol synthesis or Fischer-Tropsch production of hydrocarbons,[74,75] instead of $CO_2$; (2) atmospheric

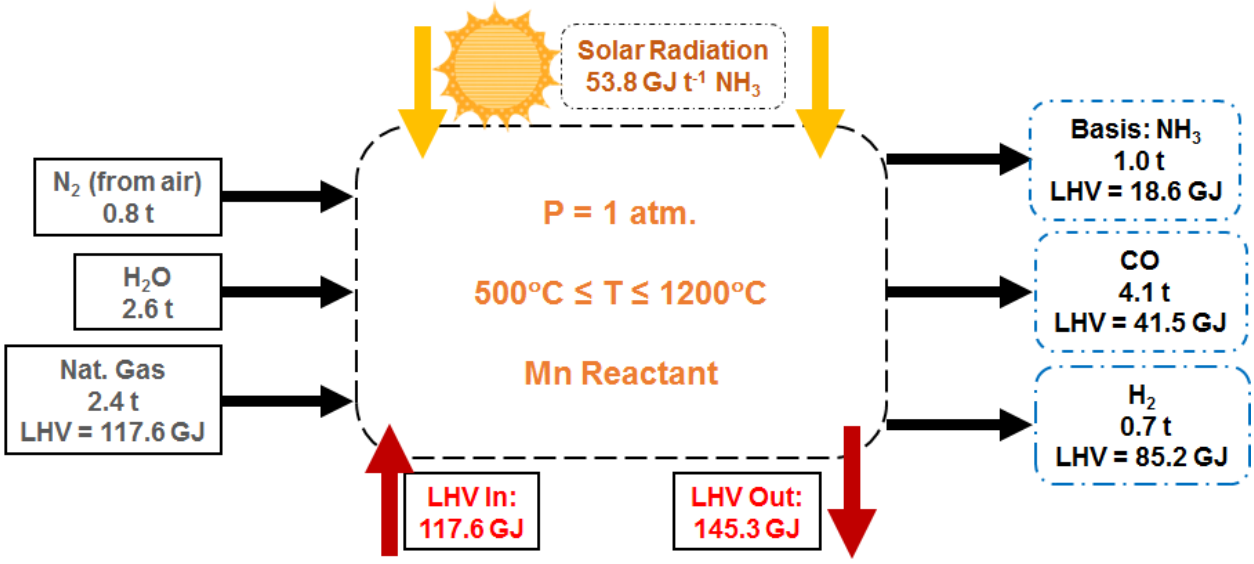


**Figure 2.2: Simplified process diagram showing step-up in energy provided in syngas (CO and $H_2$) produced over the natural gas input. LHV is lower heating value of reactants and products. Calculations are based on mass balances and reaction enthalpies, eqs (5-(8) only. Solar radiation input is calculated based solely on the energy required for the endothermic reduction reaction, eq (7). Energy required for input and exit gas conditioning and separation is neglected. Heat integration is also neglected. See published online supporting information for detailed calculations and assumptions: https://pubs.acs.org/doi/suppl/10.1021/acs.iecr.7b03173**

operating pressure vs. about 200 atmospheres for H.-B.; (3) no sensitive catalysts are used; and (4) hydrogen in $NH_3$ is derived directly from water and not fossil carbon sources. The stoichiometric $H_2$/CO molar ratio of 2 produced in the MnO reduction step is convenient for methanol synthesis,[74] but can also be used for Fischer-Tropsch synthesis[76] or simply burned to provide process heat.

An alternative strategy for nitrogen fixation to $NH_3$, which separates the simultaneous nitrogen activation and protonation performed on a heterogeneous catalyst in the H.-B. process into separate steps at different times, is demonstrated here at the gram scale. Dinitrogen is activated by chemical reaction to a metal nitride at atmospheric pressure instead of classical high-pressure heterogeneous catalysis. Renewable energy input via concentrated solar radiation, electrical heating, or alternatively via combustion of some of the produced syngas is simulated with a laboratory tube furnace to evaluate the properties of Mn pertaining to the individual steps of the proposed thermochemical cycle to produce $NH_3$. The present work contributes toward more sustainable $NH_3$ synthesis at ambient pressure with production of useful syngas instead of $CO_2$ release to the atmosphere.

## 2.4 Experimental

### 2.4.1 Materials

All gases were supplied by Matheson Tri-gas in pressurized cylinders. Pure gases ($CH_4$, $N_2$, Ar, He, $CO_2$, and $H_2$) were purchased UHP grade. Mn metal was obtained as powder from Sigma-Aldrich (No. 266132, 99% pure, -325 mesh). MnO was similarly obtained from Noah Technologies (No. 14875, 99.5% pure, -325 mesh). NaOH pellets (No. S318, certified ACS, 97% pure) and $NH_4Cl$ powder (No. A661, certified ACS, 99.5% pure) were both obtained from Fisher Chemical. Glassware was cleaned in acetone (Fisher Chemical No. A16P, histological grade) or via KOH/ethanol bath. Both the KOH pellets (No. P2501, certified ACS, 85% pure) and ethanol

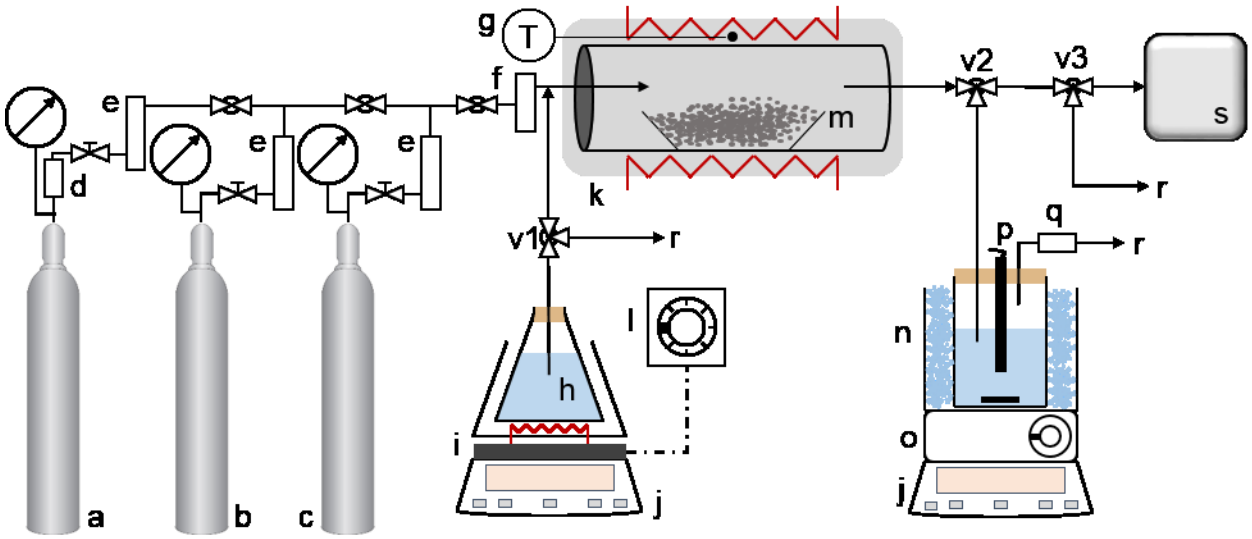


**Figure 2.3: Experimental setup for use in nitridation, corrosion, and reduction reactions: a) $CH_4$ cylinder, b) Ar cylinder, c) $N_2$ cylinder, d) flashback arrestor, e) variable area flowmeter with metering valve, f) redundant variable area flowmeter without valve, g) thermocouple, h) liquid DI $H_2O$, i) heating mantle for steam generation, j) balance, k) electric tube furnace, l) variable transformer, m) quartz boat with solid reactant, n) aqueous NaOH solution (pH > 11) in ice bath, o) stir plate, p) $NH_3$ ISE, q) Dräger $NH_3$ gas detection tube, r) gas purge to vent hood, s) 500 L gas collection bag, v) 3-way ball valves.**

(No. A405P, histological grade) were purchased from Fisher Chemical. $H_2O$ was deionized (Direct-Q 3UV, Millipore) before use as a reactant. Serial dilution of an $NH_3$ stock solution (Aqua Solutions, No. 0374-1L, 2500 ppm $NH_3$ in $H_2O$) was used for direct calibration of an $NH_3$ ion-selective electrode ($NH_3$ ISE, described below) for $NH_3$ determination. Dräger gas detection tubes (Drägerwerk AG & Co. KGaA, Germany, No. 8101941 for 5-100 ppm $NH_3$, No. CH25601 for 5-700 ppm CO, and No. CH29901 for 0.1-7 vol % CO) and the Dräger Accuro pump kit (Drägerwerk AG & Co. KGaA, Germany, No. 4053473) were used to quantify $NH_3$ in corrosion reaction gas-phase products as well as CO produced in reduction experiments. The uncertainty associated with use of Dräger tubes to quantify gas concentrations is estimated at ± 10% of the measured value.

### 2.4.2 Process Equipment

A tube furnace system (Figure 2.3) was used to achieve the temperatures and energy input for eqs (5-(8) discussed above. The solid powder reactant (Mn, Mn-nitride, and MnO) was

contained in a quartz boat (custom, in-house, 16mm ID, 80 mm length) occasionally lined with stainless steel foil (QuickShipMetals.com, 304 stainless steel, 0.002 in. thick, No. SF-1-6-60) during the corrosion step as a barrier between NaOH and the quartz boat inside the tube furnace (custom quartz tube, Technical Glass Products, 60 mm ID, 1.22 m length, Lindberg/Blue furnace and controller Nos. HTF544347C and CC58434C respectively). Pressurized gas cylinders were connected to a manifold allowing each gas to be individually and manually controlled by variable area flowmeters with attached metering valves (for $N_2$, Cole-Parmer No. EW-03229-27, for Ar and $CH_4$ Aalborg Nos. PMR1-012753 and PMR1-015787 respectively). The total flow (after gas mixing) was measured redundantly by a fourth variable area flowmeter (OMEGA No. FL-2013-NV). Steam generation was achieved by heating mantle (Glas-Col No. 0-410, 2000 mL) which was manually controlled (Powerstat Variable Autotransformer No. PN116B) and placed on top of a balance (LW Measurements, No. HRB-10001, 10 kg maximum, 0.1g accuracy) to measure the mass loss of steam sent to the furnace. The effluent stream from the corrosion step was routed through aqueous NaOH as a liquid absorbent (pH > 11) in a stirred ice bath (ThermoScientific, No. S130815) for real-time $NH_3$ detection. The entire absorbent apparatus was set on a balance (LW Measurements, No. HRB-10001, 10 kg maximum, 0.1 g accuracy) to attain a steam balance and measure incoming product and surplus reactant accumulation with each data point. The effluent stream for the reduction reaction was directed to a 500 L gas collection bag (CEL Scientific, Kynar, 3 mil) for characterization and quantification of gas products after each MnO reduction experiment. Solid reactants and products were weighed using a laboratory balance (A&D, No. GR-120, 120 g maximum, 0.1 mg accuracy).

### 2.4.3 Manganese Nitridation

Mn nitridation experiments were performed according to Figure 2.3. Mn (3.0 ± 0.1 g) was loaded into a quartz boat and preheated in a drying oven at 105-130 °C in air for 30 min to remove adsorbed water on the surface. The boat was then transferred to the tubular furnace, and a $N_2$ purge flow of 2.0 ± 0.1 $L_{(STP)}$ $min^{-1}$ ($P_{N_2} = 1$) was established for 30 min. The solid reactant was then heated from room temperature to the reaction temperature, which varied by experiment between 600 and 1000 °C, and held for reaction times varying between 30 and 240 min. The furnace heaters were then turned off and the furnace was opened for cooling by external forced air convection and by increasing the $N_2$ flow rate to 4.0 ± 0.1 $L_{(STP)}$ $min^{-1}$ to expedite sample cooling within the furnace for 15 min to near room temperature. The solid Mn-nitride product possessing the maximum fixed nitrogen content was used as the reactant for the subsequent $NH_3$ synthesis step.

### 2.4.4 Manganese Nitride Corrosion, Ammonia Harvest

$NH_3$ synthesis experiments were performed according to Figure 2.3 where the Mn-nitride reactant was the product from the previous nitridation step which possessed the maximum fixed nitrogen content. 2.0 ± 0.1 g Mn-nitride, synthesized during the nitridation step, was loaded into a quartz boat and placed in the reaction furnace. 1500 ± 20 mL of $H_2O$ was brought to a rolling boil then power was reduced to achieve the desired constant flow of 1.2 ± 0.2 g $H_2O_{(g)}$ $min^{-1}$ ($P_{H_2O} = 1$). While the steam was vented using a three-way valve, the furnace with the boat containing the Mn-nitride was purged with Ar (1.9 ± 0.2 $L_{(STP)}$ $min^{-1}$ for 30 min at room temperature, $P_{Ar} = 1$) to evacuate air. The furnace was then heated to 500 ± 5 °C while maintaining Ar flow. The total heating time was approximately 9 min. Once the reaction temperature was reached, the Ar stream was replaced by steam at 1.2 ± 0.2 g $H_2O_{(g)}$ $min^{-1}$ ($P_{H_2O} = 1$). The effluent vapor stream was condensed in an aqueous basic absorbent (NaOH in $H_2O$, pH >

11) maintained at 0 °C in an ice bath for $NH_3$ detection via $NH_3$ ISE. The cool down procedure was similar to that of the nitridation step described above, however Ar flow at 4.1 ± 0.2 $L_{(STP)}$ $min^{-1}$ ($P_{Ar} = 1$) was used as the purge gas instead of $N_2$. The solid product was removed for analysis and storage after the furnace was allowed to cool.

To overcome limited $NH_3$ yields,[77] the Mn-nitride was mixed with NaOH in a 1:1 molar ratio of NaOH:$N_{Nitride}$ to test if the addition of the Na cation facilitates $NH_3$ liberation. Samples were prepared by loading the quartz boat, now lined with stainless steel foil, with 2.0 ± 0.1 g of the Mn-nitride mixed with crushed NaOH in a 1:1 molar ratio NaOH:$N_{Nitride}$ (typically ~0.4 g NaOH). The Na-promoted corrosion experiments were then performed similarly as those described without NaOH.

### 2.4.5 Manganese Oxide Reduction

Oxide reduction experiments were conducted using a 4 vol % $CH_4$ – 96 vol % $N_2$ input stream ($P_{CH_4} = 0.04, P_{N_2} = 0.96$) while following a procedure similar to the previous steps of the cycle. Diluting $CH_4$ with $N_2$ is advantageous as it accomplishes the reduction and nitridation reactions, eqs (7) and (4) respectively, in a single process step (Figure 2.1).

Oxide reduction experiments were performed according to Figure 2.3. $CH_4$ was used as the reducing agent and was diluted to 4 vol % $CH_4$ – 96 vol % $N_2$ ($P_{CH_4} = 0.04, P_{N_2} = 0.96$) to produce the reactant gas mixture by combining the two gases in the manifold as shown in Figure 2.3 using variable area flowmeters with metering valves. 2.0 ± 0.1 g MnO, as purchased, was loaded into a quartz boat and preheated for 30 min in air in a drying oven at 105-130 °C to desorb any water on the surface. The boat with MnO was then transferred to the tubular furnace where the reducing gas purge flow was established for 30 min. The $CH_4$ and $N_2$ flowrates were 79.7 ± 8.6 $mL_{(STP)}$ $min^{-1}$ and 1.9 ± 0.1 $L_{(STP)}$ $min^{-1}$ respectively. The furnace was then heated, while

reactant gas flow was maintained, to a reaction temperature of 1150 °C. The total heating time was approximately 30 min and the furnace was held at 1150 °C for an additional 30 min after heating. Rapid cool down of the reactor was achieved by turning off the furnace, halting the $CH_4$ flow ($P_{CH_4} = 0$), increasing the $N_2$ flow to 5.2 ± 0.1 $L_{(STP)}$ $min^{-1}$ ($P_{N_2} = 1$), and following the same cool down procedure used in the nitridation step. The sample was removed and all gas flows stopped after 15 min of cooldown time. The effluent gas stream from the furnace was collected in a 500 L gas bag for analysis.

### 2.4.6 Solid State Analysis

Powder X-ray diffraction (XRD) using a Miniflex II diffractometer (Cu-target, 30 kV/15 mA output, 10-100 °2θ range, 0.5 °2θ/min scan speed, 0.02 data points/°2θ, continuous mode, Rigaku) was used for the bulk of the quantitative solid identification and analysis (PDXL software version 1.6.0.0, Rigaku) in combination with pre- and post-experiment solid masses. Phase identification was accomplished by comparison with the International Centre for Diffraction Data[78] (ICDD) PDF-2 database. All solid samples were stored in vials at room temperature under $N_2$ or Ar atmosphere.

### 2.4.7 Ammonia Detection

The $NH_3$ absorbed was detected by an ion-selective electrode ($NH_3$ ISE, Thermo Scientific Orion, No. 9512BNWP, 95% response in ≤ 1 min) and digital pH meter (OMEGA, No. PHB-62, in mV mode) in real time with negligible detection lag. The effluent stream in the corrosion step, containing $NH_{3(g)}$ and excess $H_2O_{(g)}$, was routed through an aqueous NaOH absorbent (pH > 11) chilled to 0 °C in an ice bath (Figure 2.3). Prior to each experiment the $NH_3$ ISE was calibrated directly by serial dilution of a 2500 ppm $NH_3$ in $H_2O$ stock solution. The amount of $NH_3$ recovered was determined by the $NH_3$ concentration detected by the ISE and the accumulated mass of the

absorbent. The final concentration of absorbed $NH_3$ was verified by colorimetric assay (API® Aquarium $NH_3$ Test Kit) tested on a diluted sample of expected $NH_3$ concentration. Vapor phase $NH_3$ detection was measured via a Dräger gas detection tube operated using an Accuro pump kit for repeatable measurements. The accuracy of gas detection via Dräger tubes is estimated at ± 10% of the measured value.

### 2.4.8 Gas Detection

All effluent vapors from MnO reduction experiments were captured in a 500 L gas bag for post-experiment analysis. $H_2$, $CO_2$, and remaining $CH_4$ were analyzed by gas chromatography (GC, Hewlett Packard, No. 6890, split/splitless, dual channel TCD/FID, controlled by Environmental ChemStation vD.03.00.611). The $H_2$ and $CO_2$ were tested via thermal conductivity detector (TCD, Varian Molsieve 5Å column No. CP 7534) while the $CH_4$ was tested via flame ionization detector (FID, J&W GS-GasPro column, No. 113-4332). Ar was used as the GC carrier gas for the convenience of a lower thermal conductivity relative to the thermal conductivities of the expected product gases.[73,79] This simplified peak integration. The $H_2$ peak sensitivity of the TCD was largely improved due to the advantageous thermal conductivity difference between Ar and $H_2$.[73,79] CO was measured using Dräger gas detection tubes as previously discussed.

### 2.4.9 Particle Bed Characterization

Table 2.1 shows the characterization of the solid powder beds, both before and after each reaction. $N_2$ physical adsorption was employed (Quantachrome Autosorb-1 controlled by AS1Win v1.55-B software) for surface characterization. All samples were degassed at 200 °C and $10^{-7}$ atm for greater than 5 hours before analysis. The specific surface area of each sample was calculated by the BET method[80] (11 points, $0.05 \leq P/P_0 \leq 0.30$).[81] Bulk phase information was identified using XRD as previously discussed. Maximum particle size was either specified by the

manufacturer or evaluated using a 3 in. diameter sieve set using standard screens 60 – 400 mesh (Cole-Parmer No. EW-59987).

**Table 2.1: Characterization of solid reactant and product particle beds.**

| | [a,b]Mn | [c]$Mn_4N$ ($Mn_6N_{2.58}$) | [d]$Mn_6N_{2.58}$ ($Mn_4N$) | [e]MnO ($\alpha$-$NaMnO_2$) | [f]MnO ($Mn_xN_y$) | [a,g]MnO | [h]MnO ($Mn_6N_{2.58}$) |
|---|---|---|---|---|---|---|---|
| **Space Group** | I-43m | Pm-3m ($P6_322$) | $P6_322$ (Pm-3m) | Fm-3m (C2/m) | [i]Fm-3m | Fm-3m | Fm-3m ($P6_322$) |
| **Max Particle Size (µm)[j]** | 45 | 45 | 45 | 45 | 45 | 45 | 45 |
| **BET Surface Area ($m^2$ $g^{-1}$)** | 0.966 | 1.086 | 0.446 | 2.347 | 0.667 | 2.743 | 6.805 |
| **Particle Bed Thickness (mm)[k]** | 1.0 | -- | 1.4 | -- | -- | 1.0 | -- |
| **Particle Bed Surface ($cm^2$)[l]** | 11.6 | 11.6 | 11.6 | 11.6 | 11.6 | 11.6 | 11.6 |

Superscripts as follows: a) as purchased, b) reactant for Mn-nitridation reactions, c) product of Mn-nitridation at 700 °C for 60 min, d) product of Mn-nitridation at 800 °C for 120 min and reactant for $NH_3$ harvest reaction (values do not include addition of NaOH promotor), e) product of $NH_3$ harvest reaction with NaOH promotor, f) product of $NH_3$ harvest reaction without promotor (several Mn-nitride stoichiometries are represented by $Mn_xN_y$), g) reactant for MnO reduction reaction, h) product of MnO reduction reaction, i) refers to primary component of mixture only, j) after grinding with mortar and pestle, k) applies to reactants only, uncertainty estimated at ± 0.3mm via error propagation, l) uncertainty estimated at ± 1.0 $cm^2$ via error propagation.

## 2.5 Results and Discussion

### 2.5.1 Manganese Nitridation

The optimum condition to immobilize 8.7 ± 0.9 wt. % N in Mn at 1 atm ($P_{N_2} = 1$) mainly as $Mn_6N_{2.58}$ was 120 min at 800 °C (particle size about 44 µm). This time can likely be significantly reduced to the order of tens of minutes by reducing the particle size, or even to minutes or seconds using nanoscale particles since nitrogen diffusion through solid Mn and the nitride product shell likely limit nitridation.[82]

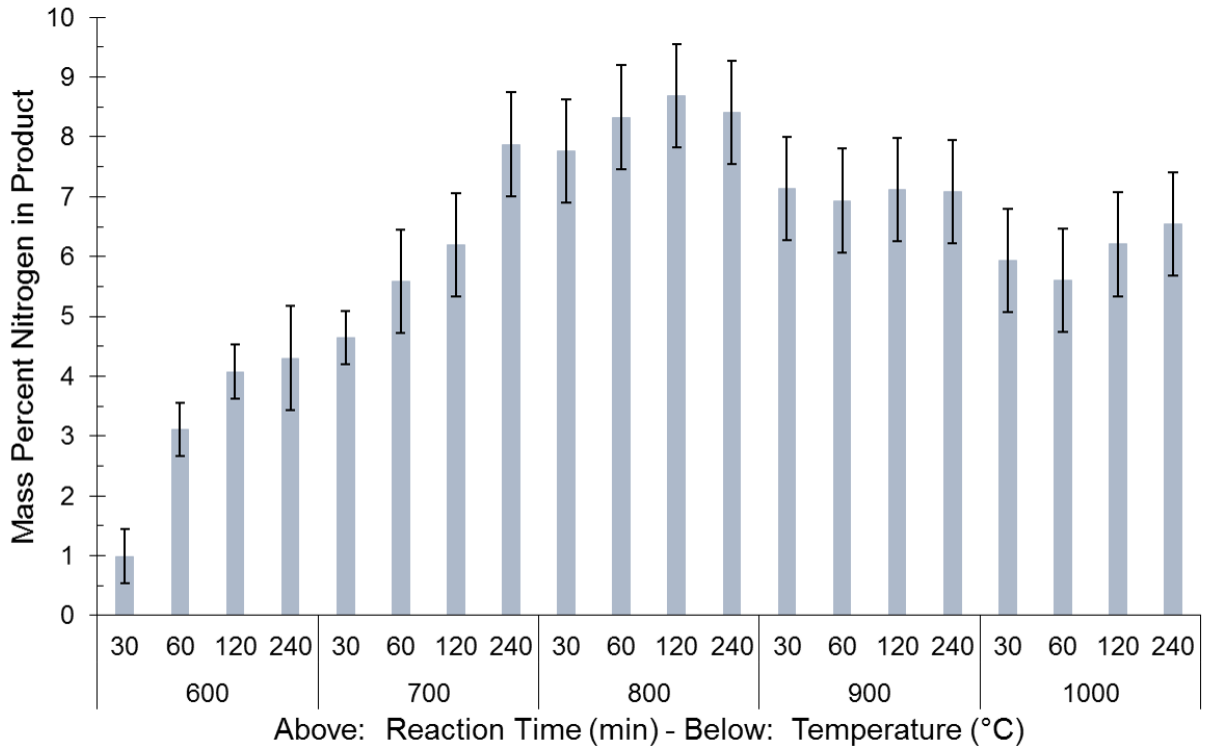


**Figure 2.4: Nitrogen content of solid products from nitridation reactions performed at 1 atm $N_2$. Error bars are from error propagation.**

Figure 2.4 and Figure 2.5 show the results for Mn nitridation experiments (1 atm $N_2$, 600-1000 °C, according to the procedure in Figure 2.3). At 600 °C nitrogen fixation appears to be kinetically limited as 32.3 ± 7.5 wt. % of the Mn remains unconverted after 2 hours. Mn conversion significantly improves after increasing the temperature to 700 °C where only 8.1 ± 7.5 wt. % of the Mn remains after 30 min and $Mn_4N$ (N/Mn ratio of 0.25) is the only nitride product. At 700 °C and 1 hour the remaining Mn is converted to $Mn_4N$ however $Mn_6N_{2.58}$ (N/Mn ratio of 0.43) exists as a minor product. An additional hour at 700 °C increases the $Mn_6N_{2.58}$ fraction by a factor greater than 13, decreases the fraction of $Mn_4N$, and further confirms that $Mn_6N_{2.58}$, having the larger N/Mn ratio, is the product of nitridation of $Mn_4N$ and not a direct product of Mn nitridation.[83] The $Mn_4N$ and hexagonal $Mn_6N_{2.58}$ phases reported here are consistent with the Mn-

N phase diagram where $Mn_6N_{2.58}$ is the anticipated product from further nitridation of $Mn_4N$.[84] This behavior is similar to that of other interstitial nitride transformations such as $Cr_2N$ to CrN.[52] $Mn_6N_{2.58}$, with the higher N/Mn ratio, becomes the major product after 2 hours at 800 °C. This yields the maximum fixed nitrogen at this temperature. Above 800 °C fixed nitrogen yields decrease even as residence times increase.

Figure 2.6 shows the XRD spectra for the reaction products at 800 °C for 120 min, 700 °C for 60 min, and the reactant Mn as purchased. The post-reaction spectra both show mixtures of $Mn_4N$, $Mn_6N_{2.58}$, as well as MnO (likely from residual $O_2$ remaining in the reactor after the initial gas purge). The product after 60 min at 700 °C is a nitride mixture rich in $Mn_4N$ (90.8 ± 7.5 wt.% $Mn_4N$) while the product after 120 min at 800 °C is a nitride mixture rich in $Mn_6N_{2.58}$ (82.1 ± 7.5 wt.% $Mn_6N_{2.58}$). $Mn_6N_{2.58}$ is the preferable stoichiometry as the N/Mn ratio is 1.72 times larger than that for $Mn_4N$. Unfortunately, $Mn_6N_{2.58}$ is not detected at any temperature without at least some $Mn_4N$. Maximum nitrogen fixation of 8.7 ± 0.9 wt. % N occurs at 800 °C and 120 min

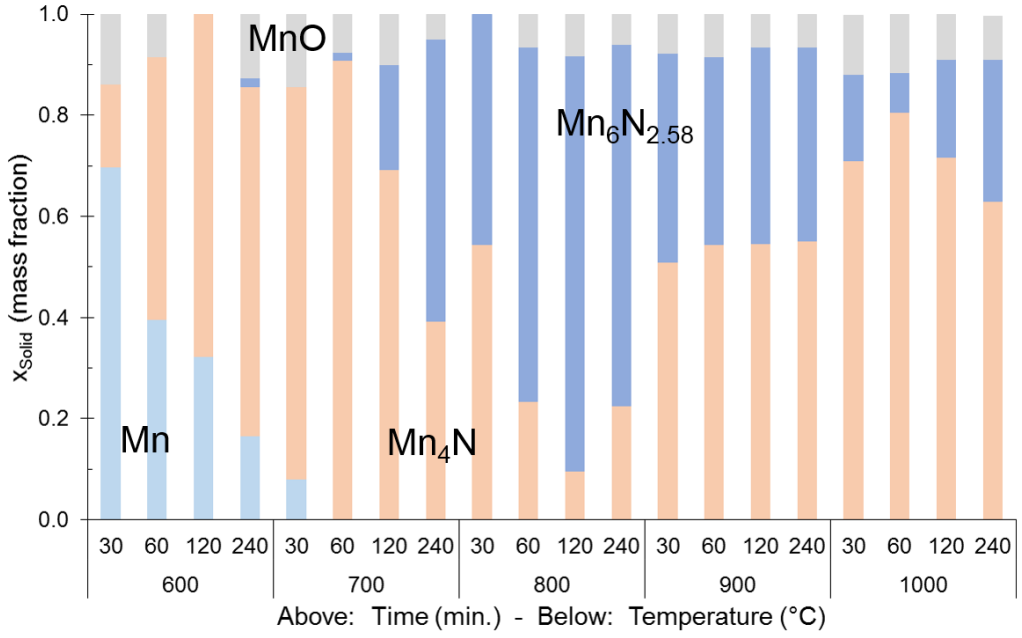


**Figure 2.5: Nitride product yields detected by XRD after nitridation experiments performed at 1 atm $N_2$. Uncertainty is estimated at ± 0.075 for each phase.**

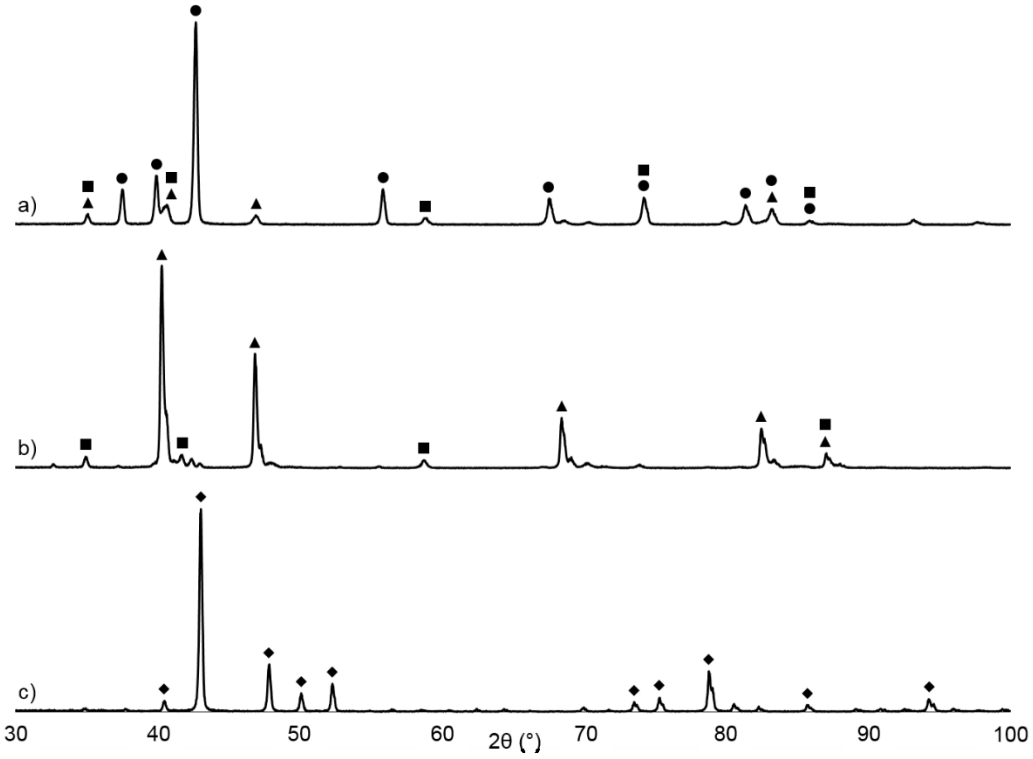


**Figure 2.6: Selected XRD spectra relating to Mn nitridation: a) product from reaction at 800 °C for 120 min; b) product from 700 °C at 60 min; and c) Mn reactant as purchased. The major peaks of each spectrum are: (●) $Mn_6N_{2.58}$ (ICDD PDF No. 01-071-0200), (▲) $Mn_4N$ (ICDD PDF No. 01-089-4804), (■) MnO (ICDD PDF No. 01-078-0424), (♦) Mn (ICDD PDF No. 00-032-0637).**

where both $Mn_6N_{2.58}$ and $Mn_4N$ stoichiometries are observed. Pure $Mn_6N_{2.58}$ would correspond to 9.9 wt. % nitrogen. The harvesting of $NH_3$ from the Mn-nitride will be described below.

### 2.5.2 Manganese Nitride Corrosion, Ammonia Harvest

$NH_3$ liberation from Mn-nitride corrosion with steam was found to be significantly improved by addition of NaOH as a promotor. The definitions of conversion and yield used can be found in the literature.[85] At 500 °C and 1 atm steam ($P_{H_2O} = 1$), $NH_3$ yield from the Mn-nitride alone is limited to 0.04 after 120 min. Addition of NaOH to the nitride reactant increased $NH_3$ yield to 0.54 over the same time. The Na cation is thought to act as an electronic promotor to balance the competing requirements of the successive redox reactions undergone by the solid Mn

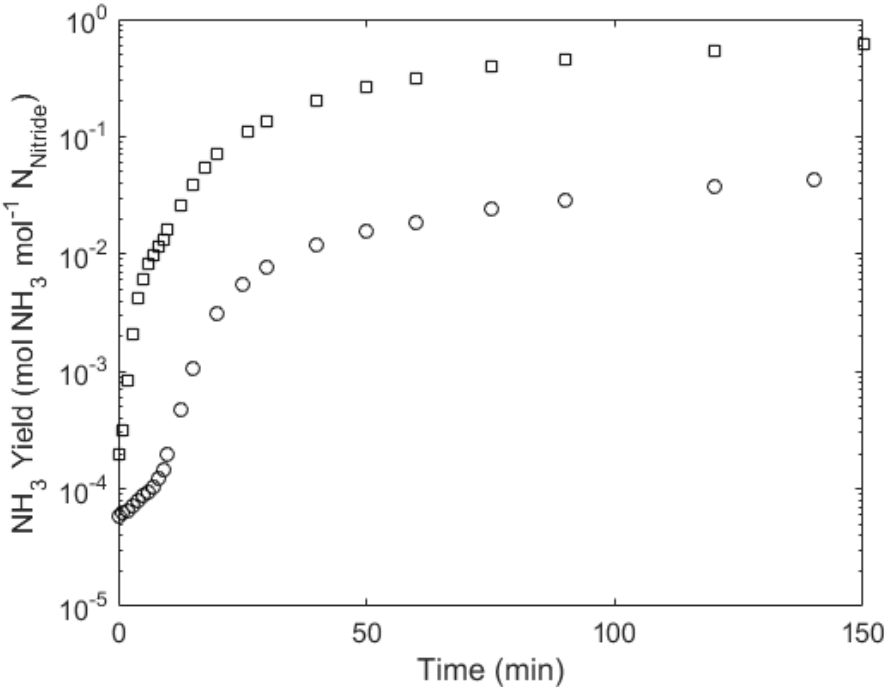


**Figure 2.7: $NH_3$ synthesis via steam corrosion of Mn-nitride: (□) with addition of NaOH promotor and (○) without NaOH promotor.**

reactant to produce the desired products under technically feasible and economically favorable conditions.[77]

Mn-nitride was prepared at 800 °C for 120 min (above). The $Mn_6N_{2.58}$-rich nitride mixture was then reacted with steam at 500 °C to produce $NH_3$ according to Figure 2.3. The Na-promoted nitride reactant was obtained by mixing ground NaOH with the $Mn_6N_{2.58}$-rich nitride mixture in a 1:1 molar ratio NaOH:$N_{Nitride}$ prior to the corrosion reaction. The results are shown in Figure 2.7.

Thermochemical data suggests the reaction between steam and $Mn_5N_2$ may liberate nitrogen as $NH_3$ below temperatures of 180 °C.[71,72] Unfortunately $NH_3$ formation is limited by very slow kinetics at this temperature, while above 180 °C the $NH_3$ decomposition products $N_2$ and $H_2$ become thermodynamically preferred. However the results from Figure 2.7 confirm $NH_3$ is metastable above 180 °C and can be recovered.[60] Equilibrium thermodynamic calculations are based on closed systems and infinite time scales.[86] However the open flow reactor described by

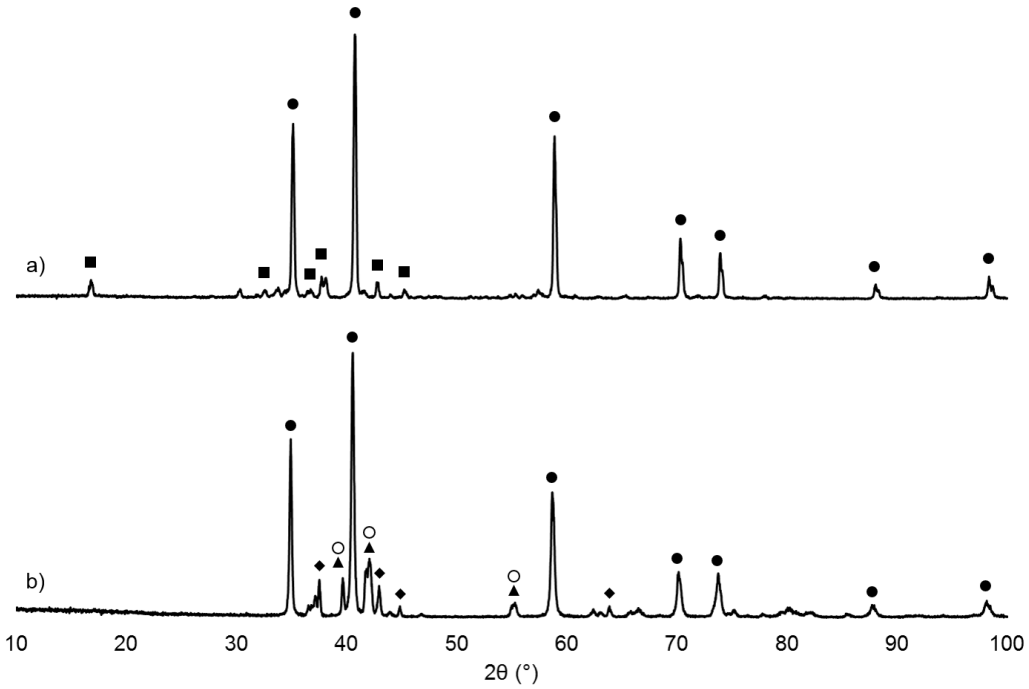


**Figure 2.8: XRD spectra of the solid products from Mn-nitride corrosion with steam at 500 °C: a) with NaOH promotor added in 1:1 molar ratio NaOH:$N_{Nitride}$ and 360 min reaction time and b) without NaOH promotor after 140 min reaction time. The major peaks in each spectrum are: (●) MnO (ICDD PDF No. 01-078-0424), (■) α-$NaMnO_2$ (ICDD PDF No. 01-072-0830), (▲) $Mn_2N$ (ICDD PDF No. 01-074-6805), (♦) $Mn_3N_2$ (ICDD PDF No. 01-074-8391), and (○) $Mn_6N_{2.58}$ (ICDD PDF No. 00-031-0824).**

Figure 2.3, in which $NH_3$ is removed and cooled shortly after formation, stabilized the $NH_3$ product before decomposition.

The Na-promoted Mn-nitride increased the $NH_3$ yield to 0.54 in 120 min over 0.04 for the native Mn-nitride. The Na is hypothesized to act as an electronic promotor similar to the K-promoted Fe catalyst employed by the H.-B. process. That is, addition of Na may function to weaken the Mn-N forces allowing more nitrogen liberation to $NH_3$.[77] Indeed Figure 2.7 shows the case of Na-promoted $NH_3$ synthesis increased the $NH_3$ yield by a factor of 13.5 at 120 min over the case of $NH_3$ synthesis from the Mn-nitride alone. It is important to point out that the NaOH only provides enough hydrogen to stoichiometrically achieve an $NH_3$ yield of 0.33 since it is

supplied in a 1:1 molar ratio of NaOH:$N_{Nitride}$. This shows that NaOH is not providing an alternative hydrogen source but is instead altering the nature of the solid reactant.

Figure 2.8 shows the XRD spectra of the solid products for the $NH_3$ synthesis reaction at 500 °C from both the Na-promoted and native Mn-nitride cases. The Na-promoted Mn-nitride reactant, shown after 360 min reaction time, appears to completely convert as no nitrogen is detected in the final product composition. Here the primary components are identified as MnO and α-$NaMnO_2$. The native Mn-nitride reactant, shown after 140 min reaction time, still shows nitrogen remaining in the solid lattice. The main product is also MnO, however the Mn-nitride has partially rearranged to form $Mn_3N_2$ and $Mn_2N$, while $Mn_6N_{2.58}$ is also detected.

Adding ground NaOH as an electronic promotor to the Mn-nitride for reaction with steam for $NH_3$ synthesis at 500 °C increased $NH_3$ yield by a factor of 13.5 compared to absence of the promotor, over 120 min. The addition of NaOH does not supply enough hydrogen to balance the increased $NH_3$ yields yet allows more complete harvest of $NH_3$. Recycling of the MnO product, necessary to complete the cycle, will be described next.

### 2.5.3 Manganese Oxide Reduction

Conversion of MnO, as purchased, was 0.371 ± 0.072 and the yield of $Mn_6N_{2.58}$ was 0.381 ± 0.083 when a 4 vol % $CH_4$ – 96 vol % $N_2$ ($P_{CH_4} = 0.04, P_{N_2} = 0.96$) gas stream at atmospheric pressure ($P_{Total} = 1\ atm$) was contacted with MnO at 1150 °C for 30 min according to Figure 2.3. Within limits of detectability, the product gases consisted only of CO, $H_2$, and unreacted $CH_4$. $CO_2$ was not detected in the product stream.

Reducing or recycling MnO to remake Mn (or Mn-nitride), ideally with a gaseous reducing reactant,[52] is necessary to close the nitride-based $NH_3$ synthesis cycle.[66] However MnO reduction by $CH_4$ to Mn is not trivial. Thermochemistry predicts that MnO reduction by $CH_4$

becomes spontaneous around 1059 °C, while reduction by $H_2$ requires significantly higher temperatures.[71] Meanwhile $CH_4$ decomposition becomes spontaneous above 530 °C[71] and the reaction between amorphous carbon and MnO can yield $Mn_7C_3$ above 928 °C[71,87]. Undesirable carbide formation has shown to be a significant problem as the equilibrium constant, for the $Mn_7C_3$ product is 114 and 1075 at 1100 °C and 1200 °C respectively,[87] strongly favoring carbide formation and inhibiting Mn recovery. Precise control over the reaction temperature, gas flow rates and concentrations is paramount in controlling the unwanted side reactions.

Figure 2.9 shows the XRD spectra for the reduction product mixture of $Mn_6N_{2.58}$ and unreacted MnO, together with the original MnO reactant as purchased. Here it appears the MnO is initially reduced by the $CH_4$ in the gas stream to form Mn which then reacts with the $N_2$ to form $Mn_6N_{2.58}$. The benefit is that the reduction and nitridation reactions are performed simultaneously

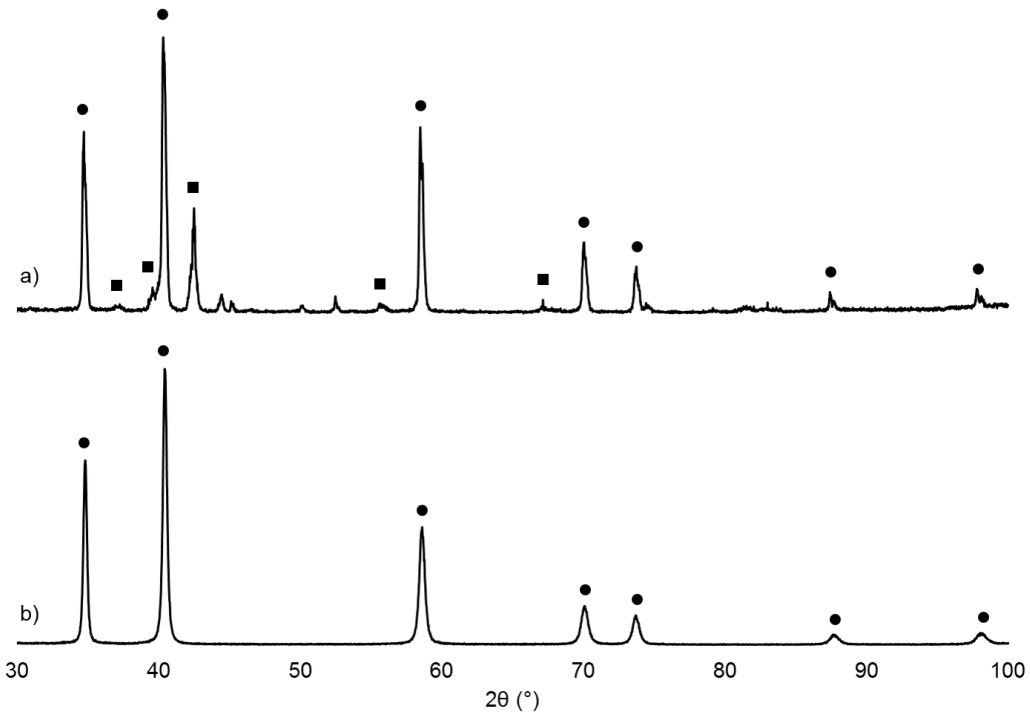


**Figure 2.9: XRD spectra of a) product mixture from MnO reduction by contact with a 4 vol % $CH_4$ – 96 vol % $N_2$ stream ($P_{CH4}$ = 0.04, $P_{N2}$ = 0.96) for 30 min at 1150 °C, and b) MnO reactant as purchased. The major peaks are: (●) MnO (ICDD PDF No. 01-078-0424) and (■) $Mn_6N_{2.58}$ (ICDD PDF No. 01-071-0200).**

during the same process step (Figure 2.1). The total MnO conversion during the 30 min reaction was 0.371 ± 0.072 and the $Mn_6N_{2.58}$ yield was 0.381 ± 0.083. Stopping the reaction after only 30 min prevented the development of the undesired product $Mn_7C_3$ which occurs due to MnO reaction with amorphous carbon deposited from $CH_4$ decomposition. The thermodynamically predicted product gases, CO and $H_2$, are confirmed. The detected syngas was 29.9 ± 6.0 mol $H_2$ $mol^{-1}$ CO. The additional $H_2$ arises as the product of the undesired $CH_4$ decomposition reaction before contact with MnO. $CO_2$ was not detected within the product stream.

Reducing MnO using a 4 vol % $CH_4$ – 96 vol % $N_2$ ($P_{CH_4} = 0.04, P_{N_2} = 0.96$) reactant gas stream does yield 0.381 ± 0.082 $Mn_6N_{2.58}$ at 1150 °C if reaction time is limited. The amorphous carbon product from $CH_4$ decomposition leads to the formation of undesirable $Mn_7C_3$ as a product. Further reducing the input $CH_4$ partial pressure, increasing the gas flow rate (decreasing $CH_4$ residence time in the reactor), and optimizing temperature may reduce carbide formation (by reducing amorphous carbon deposition from $CH_4$ decomposition) and improve $Mn_6N_{2.58}$ yield. It may also be possible to improve nitride selectivity over carbide by co-feeding $H_2$ and/or $CO_2$ with the reducing gas stream. The presence of $H_2$ will shift the equilibrium of the $CH_4$ decomposition reaction toward $CH_4$ and away from the solid carbon product, according to Le Châtelier's principle,[28] thereby limiting Mn-carbide formation. Co-fed $CO_2$ may react with any solid carbon from $CH_4$ decomposition in the reverse Boudouard reaction yielding more CO. The reverse Boudouard reaction becomes spontaneous above 707 °C.[71] The syngas product represents a step up in lower heating value, over the natural gas input, of 9.1 GJ $t^{-1}$ $NH_3$ produced.[73] It can potentially be used for Fischer-Tropsch, methanol synthesis, or simply burned as a source of process heat.

## 2.6 Conclusion

The cycled reactant necessary for sustainable $NH_3$ production via a solar thermochemical reaction cycle as proposed here will likely consist of two or more chemical elements to effectively balance the competing requirements of the nitridation, corrosion, and reduction reactions.

Mn was shown to readily fix nitrogen at atmospheric pressure ($P_{N_2} = 1$) with complete conversion occurring within 120 min between 700 and 1000 °C. After 1 hour at 700 °C all Mn was converted to $Mn_4N$ with a small amount of $Mn_6N_{2.58}$ detected. The maximum amount of fixed nitrogen occurred (8.7 ± 0.9 wt. %) after 120 min at 800 °C where $Mn_6N_{2.58}$ was the dominant product and a small amount of $Mn_4N$ remained. Further increasing reaction temperature or time did not increase fixed nitrogen yields.

$NH_3$ yield from steam corrosion of a $Mn_6N_{2.58}$-rich nitride mixture at 500 °C and atmospheric pressure ($P_{H_2O} = 1$) was limited to 0.04 after 120 min. Adding NaOH in a 1:1 molar ratio $NaOH:N_{Nitride}$ to the $Mn_6N_{2.58}$-rich nitride sample improved $NH_3$ yield to 0.54 under the same conditions. The Na is thought to function as an electronic promotor similar to H.-B. process catalysts by weakening the Mn-N forces and allowing more nitrogen liberation to $NH_3$.

Reduction of MnO to $Mn_6N_{2.58}$ was achieved using a 4 vol % $CH_4$ – 96 vol % $N_2$ ($P_{CH_4} = 0.04, P_{N_2} = 0.96$) stream. After 30 min at 1150 °C MnO conversion was 0.371 ± 0.072 and $Mn_6N_{2.58}$ yield was 0.381 ± 0.083. The thermodynamically predicted syngas coproduct was detected at a molar ratio of 29.9 ± 6.0 mol $H_2$ $mol^{-1}$ CO. 2 mol $H_2$ $mol^{-1}$ CO is the stoichiometrically predicted ratio of syngas components. The excess $H_2$ is from the undesired $CH_4$ decomposition reaction. $Mn_7C_3$ was observed due to unwanted $CH_4$ decomposition followed by reaction of MnO with the solid carbon. Careful control over all reaction parameters was necessary to limit these unwanted side reactions. $CO_2$ was not detected in the product stream.

The syngas coproduct represents a step-up of 9.1 GJ $t^{-1}$ $NH_3$ over the natural gas input based on the lower heating value of each gas. This energy upgrade represents a benefit of the thermochemical process compared to the H.-B. process which converts natural gas into worthless $CO_2$. The solar process can then be considered to store intermittent solar radiation in the form of chemical energy. Assuming 1000 kg Mn used in a cyclical process (nitridation – $NH_3$ harvest – oxide reduction – nitridation) one could perhaps estimate to convert on the order of several hundred to a few thousand kg of nitrogen per day and per ton of Mn to $NH_3$. Smaller particles, perhaps in a packed bed configuration or distributed on a porous support, can likely shorten the required time significantly due to the increased solid surface area available to reactant gases per mass of Mn and the strong dependence of diffusion-based "loading" of the manganese with nitrogen atoms on particle size. Nitride-based synthesis of $NH_3$ at atmospheric pressure shows promise, converting renewable solar energy into $NH_3$ for fertilizer as well as syngas for fuels or chemicals.

# Chapter 3 - The Kinetics of Manganese Nitridation at Atmospheric Pressure

## 3.1 Introduction

Fundamental to any ammonia ($NH_3$) synthesis cycle is the fixation of nitrogen to the cycled metal reactant, in this case Mn. It is the necessary first step. The goal in nitridation for $NH_3$ synthesis is to load the metal reactant with as much nitrogen as possible. This nitrogen can, in turn, be protonated to $NH_3$ in the next step of the cycle. Right away it is clear the efficacy of an $NH_3$ synthesis cycle will require a cycled reactant which can readily fix nitrogen. Clearly any nitrogen which fails to load into the metal, eq (2), will be unavailable to hydrogen and will not convert to $NH_3$ in the subsequent step, eq (3).

### 3.1.1 The Manganese-Nitrogen System

The thermodynamic behavior of the Mn-N phase diagram has been studied for decades yet remains unsettled.[88] Furthermore, even less is known about many of the individual Mn-N phases[84] – of which there are dozens.[88,89] Thermochemical data is only available for 2 manganese nitrides, $Mn_4N$ and $Mn_5N_2$.[71,72]

Figure 3.1 shows the *calculated* (based on the limited thermochemical data) equilibrium molar composition upon input of 10

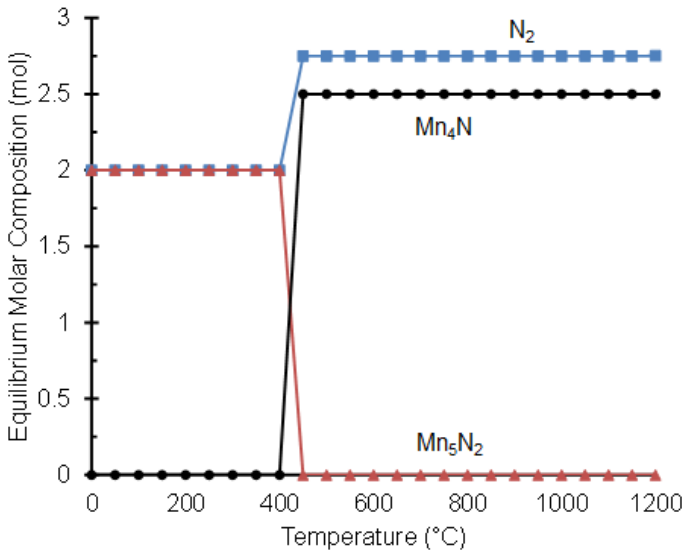


**Figure 3.1: Equilibrium molar calculations illustrating the lack of quality thermochemical data for the Mn-N system. Composition based on 10 mol Mn and 4 mol $N_2$ input into a closed system.**

mol Mn and 4 mol $N_2$ into a closed system.[90] $Mn_5N_2$ is yielded at all temperatures below 400 °C, while $Mn_4N$ is the product at all temperatures above. Figure 3.1 represents the problem with the thermochemical analysis of the Mn-N system. For example the sudden switch in stoichiometry at 400 °C is likely unrealistic and it doesn't mention the other stoichiometries observed such as $Mn_6N_{2.58}$. Any further evaluation of Mn as a reactant in thermochemical $NH_3$ synthesis will require trial and error.

## 3.2 Experimental Section

### 3.2.1 Materials

Mn metal powders were purchased from Sigma Aldrich (No. 266132, 99% pure, -325 mesh), Alfa Aesar (45098, 99.6% pure, APS < 10 μm), and Acros Organics (AC317442500, 99+%, -40 mesh). These Mn powders correspond to approximately 44, 10, and 420 μm respectively. MnO (No. 14875, 99.5% pure, -325 mesh) was purchased from Noah Technologies. UHP-grade $N_2$ was supplied in pressurized cylinders by Matheson Tri-Gas, Inc. Glassware, custom quartzware, and alumina combustion boats (described below) were cleaned with Micro-90 cleaning solution (Cole-Parmer No. EW-18100-04), acetone (Fisher Chemical, No. A16P, histological grade), ethanol (Fisher Chemical No. A405P, histological grade), KOH (Fisher Chemical No. P2501, certified ACS, 85% pure) in ethanol bath, and/or 0.1M HCl (Fisher Chemical No. A144, certified ACS Plus) solution.

### 3.2.2 Process Equipment

The experimental equipment used for the nitriding of Mn powder is shown in Figure 3.2. $N_2$, controlled manually via variable area flowmeter with attached metering valve (Cole-Parmer No. EW-03229-27), was conditioned with a high-capacity $O_2/H_2O$ trap (Restek No. 20600) before delivery to an electric tube furnace (Lindberg/Blue Nos. HTF54434C and CC58434C for the

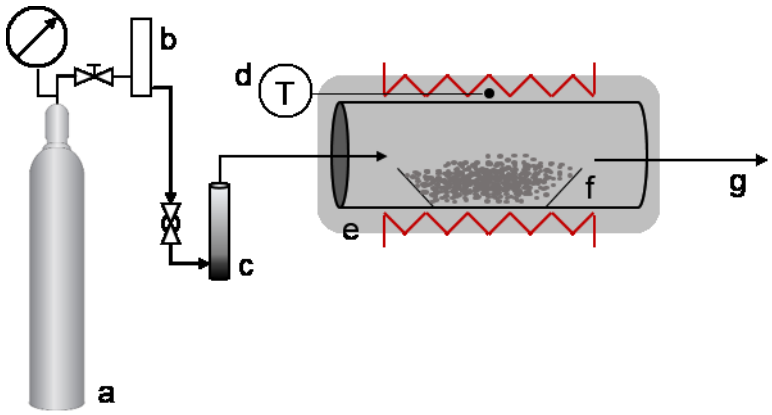


**Figure 3.2: Experimental setup for use in the Mn-nitridation reaction: a) $N_2$ cylinder, b) rotameter with metering valve, c) high capacity $O_2/H_2O$ trap, d) thermocouple, e) electric tube furnace, f) quartz or alumina combustion boat with Mn reactant, g) gas purge to fume hood.**

furnace and controller respectively; clear quartz tube, 50 mm OD, 1.22 m length, Technical Glass Products; capped by vacuum fittings, A&N Corp. Nos. 1000022 and 4000198) .

The Mn reactant was confined to a quartz (custom, in-house, 16 mm ID, 80 mm length) or alumina combustion boat (CoorsTek No. 65566, AD-998 high-alumina, 20 mL capacity) periodically lined with Cu (Alfa Aesar No. 46986, annealed, uncoated, 0.001 in thick) or stainless steel (QuickShipMetals.com No. SF-1-6-60, 304 stainless steel, 0.002 in. thick) foils. A laboratory balance (A&D, No. GR-120, 120 g maximum, 0.1 mg accuracy) was used to weigh solid reactants and products.

### 3.2.3 Manganese Nitridation

The Mn reactant (3.0 ± 0.1 g) was preheated in a drying oven ($T_{sp}$ = 115 ± 10 °C) for 30 min to desorb any surface $H_2O$ prior to placement into the tube furnace. After insertion of Mn, the tube furnace was purged with 2.0 ± 0.1 $L_{(STP)}$ $min^{-1}$ of $N_2$ ($P_{N2}$ = 1) for 30 min to remove atmospheric $O_2$. The furnace was then heated to the reaction temperature which varied by experiment between 600 and 800 °C. The furnace was then held at temperature for the reaction time varying between 5 and 240 min by experiment. The furnace was then halted, opened, and

cooled via forced air convection. Additionally the $N_2$ flow rate was doubled to 4.0 ± 0.1 $L_{(STP)}$ $min^{-1}$ for at least 15 min to assist in rapid cooldown to room temperature for analysis.

### 3.2.4 Solid State Analysis

Quantitative solid product phase identification was accomplished via powder x-ray diffraction (XRD) using a Miniflex II x-ray diffractometer (Rigaku, Cu-target, 30 kV/15 mA output, 10 - 100° 2θ range for the other 2 Mn reactants, 0.5 ° 2θ $min^{-1}$ scan speed, continuous mode) combined with solid masses before and after each experiment. Solid phase identification was achieved via comparison of experimental spectra with the Powder Diffraction File (PDF-2) database of the International Centre for Diffraction Data (ICDD).[78] Solid samples were stored under $N_2$ at room temperature.

## 3.3 Results and Discussion

### 3.3.1 Nitrogen Fixation to Manganese

Figure 3.3 shows the chemical conversion and nitrogen weight gain for Manganese at 600, 700, and 800 °C for the 10, 44, and 420 μm Mn reactant particles. The data confirms the Mn-N phase diagram where equilibrium nitrogen fixation decreases with increasing temperature.[89] Yet rate of nitrogen fixation increases with both increasing temperature and decreasing particle size. The known reaction pathway for Mn nitridation at atmospheric pressure is shown in eq (9). From the Mn-N phase diagram,[84] as well as previous experimentation,[46,83] it is expected that ζ-$Mn_6N_{2.58}$ is formed by further reaction of ε-$Mn_4N$ with $N_2$. The nitride yield (either $Mn_4N$ or $Mn_6N_{2.58}$), $Y_{Nitride}$, and Manganese conversion, $X_{Mn}$, are determined by eq (10).[85]

$$6Mn + 1.29N_2 \leftrightarrow \frac{3}{2}Mn_4N + 0.54N_2 \leftrightarrow 1Mn_6N_{2.58} \quad (9)$$

$$Y_{Nitride} = \frac{n^t_{Mn,Prod}}{n^0_{Mn}} \qquad X_{Mn} = \frac{n^0_{Mn} - n^t_{Mn}}{n^0_{Mn}} \quad (10)$$

Where $n^t_{Mn,Prod}$ represents the mol of Mn in the nitride product, and $n^0_{Mn}$ is the mole of Mn reactant.

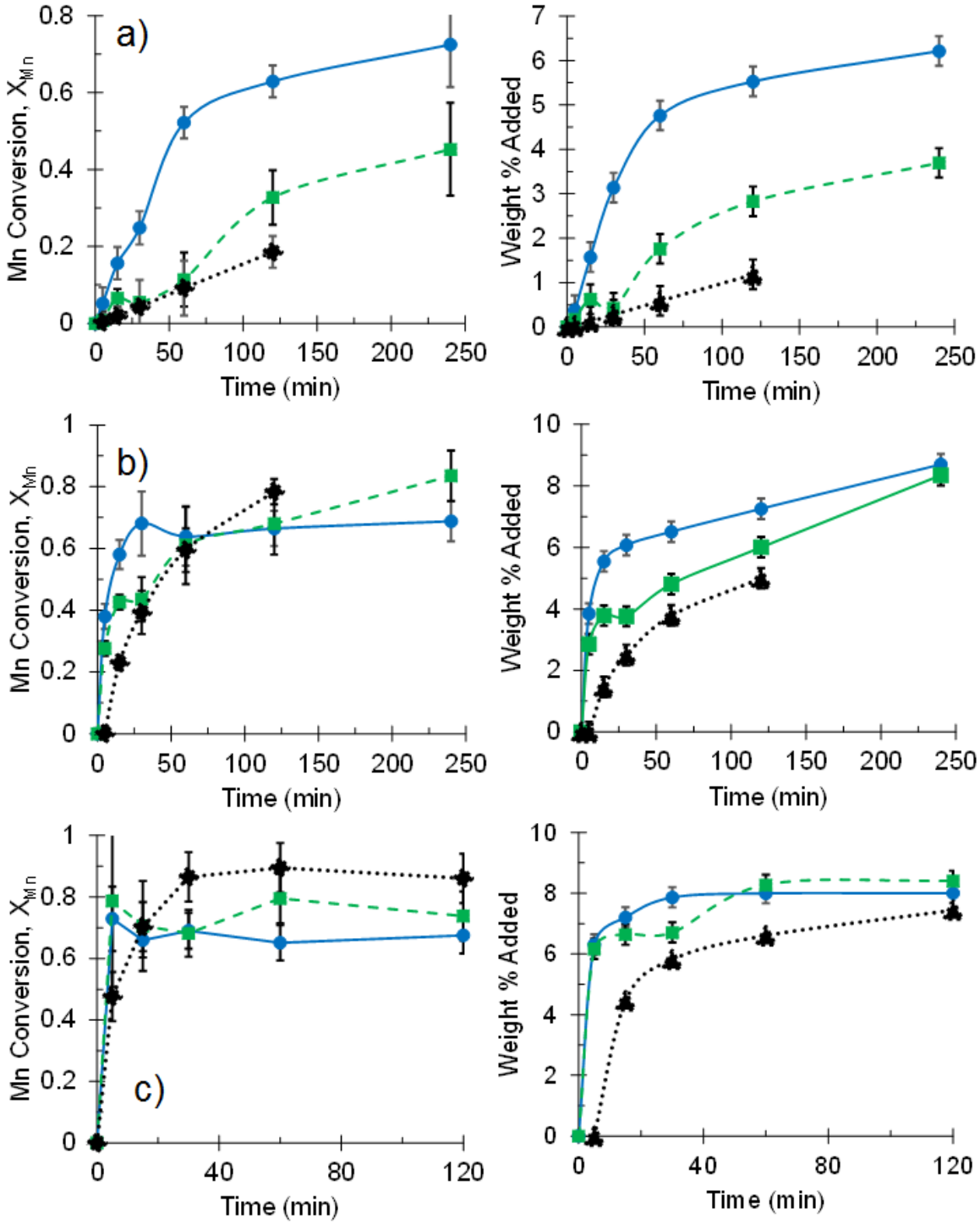


**Figure 3.3: Chemical conversion charts and mass increase data for the isothermal nitridation of Manganese. Rows a, b, and c correspond to 600, 700, and 800 °C respectively. The black dashed line, green squares, and the blue circles each correspond to the 420, 44, and 10 µm-sized powders. Error bars are from error propagation. The uncertainty on the abscissa is estimated at ± 2 min. Data includes a small amount of unavoidable oxygen present. MnO yields were at most $Y_{MnO} = 0.0849 \pm 0.0104$, and were typically lower.**

As one might expect, at 600 °C, the 10 µm Mn particles exhibits the better yields. This data confirms the Mn-N phase diagram[89] in that a larger percentage of Mn atoms will eventually convert to nitride at lower temperatures. However, the 420 µm and even the 44 µm Mn particles are quite slow to react at this temperature. Additionally the linear shape of the 420 µm nitridation curve suggests that chemical kinetics are governing the large-particle regime over mass-transfer limitations at this temperature.

Consider the runs which occurred at 700 °C (b in Figure 3.3). For the smallest particle size, the maximum amount of Mn is fixed in no more than 30 min. However, the mass of nitrogen fixed continues to increase over the remaining 3.5 hours. The rationale for this paradox stems from the transition from ε-$Mn_4N$ to ζ-$Mn_6N_{2.58}$ discussed above. The N/Mn ratio for $Mn_4N$ is 0.25 while the N/Mn ratio for $Mn_6N_{2.58}$ is 0.43. Which correspond to a Mn/N ratio of 4 and approximately 2.33 respectively. As temperature increases, nitrogen fixation to Mn transitions from a regime governed by kinetics to one of thermodynamic limitations. That is, the driving force reaches a limiting value at a given concentration of N in Mn (without inducing a phase change, increasing the $N_2$ pressure, or otherwise altering the system). Knowing this, the transition from a lower N/Mn ratio product ($Mn_4N$) to a product possessing a greater N/M ratio ($Mn_6N_{2.58}$) means the simultaneous transition is occurring from a product of higher Mn/N ratio to one of a lower Mn/N ratio.

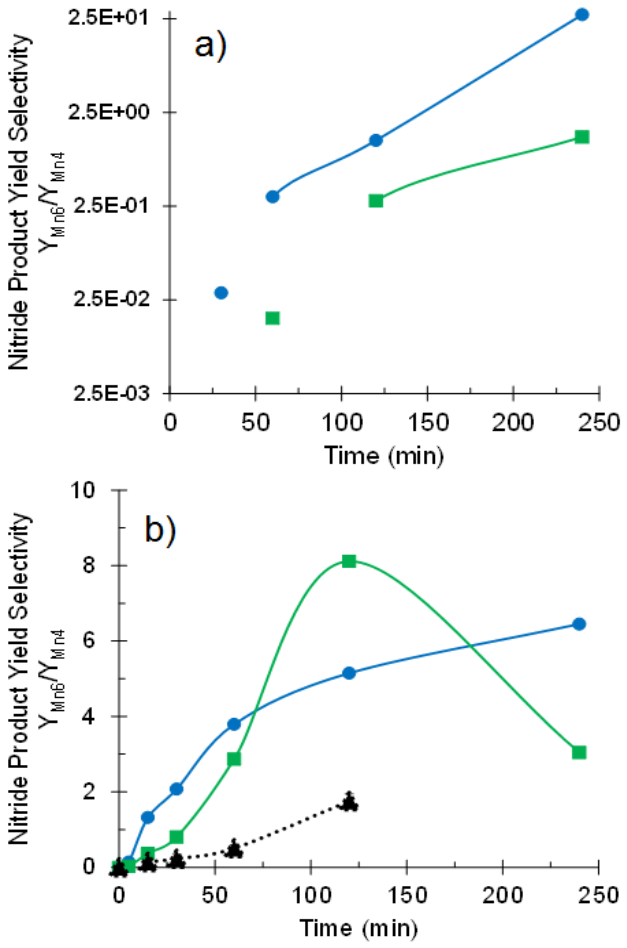


**Figure 3.4: Nitride product selectivities from nitrogen fixation to Manganese at a) 700 °C and b) 800 °C. As in Figure 3.3, the blue circles, green squares, and black triangles represent 10, 44, and 420 µm particle sizes respectively. Error on the ordinate is estimated at approximately 10% of the value in question.**

When considering the solar thermochemical cycle discussed in this work, it is perhaps more important to consider the mass of nitrogen fixed to the metal over which nitride product is actually formed. An original goal was to prefer the nitride with greater N/Mn ratio as it would allow for more N to be fixed per mass of Mn. However this is really only true of all of the Mn actually converts. It is clear from Figure 3.3 that as much as 30 mol% of the Mn remains unconverted. The overall $Mn_6N_{2.58}/Mn_4N$ selectivities of the reaction at 700 and 800 °C are plotted in Figure 3.4 for the 10 and 44 μm Mn particles. The selectivity (S) is defined here as the ratio of product yields and it is defined here according to eq (11). At 700 °C, the large particles did not form $Mn_6N_{2.58}$ enough at these temperatures to warrant their inclusion.

$$S_{Mn_6/Mn_4} = \frac{Y_{Mn_6N_{2.58}}}{Y_{Mn_4N}} \tag{11}$$

Increasing the temperature to 800 °C allows for rapid fixation of nitrogen to the manganese. However the equilibrium is reached rather quickly, within approximately 30 min, for all 3 particle sizes. An interesting development is that reducing the particle size appears to decrease the equilibrium Mn conversion slightly as defined in eq (10). Referring to Figure 3.3, at 600 °C (a)

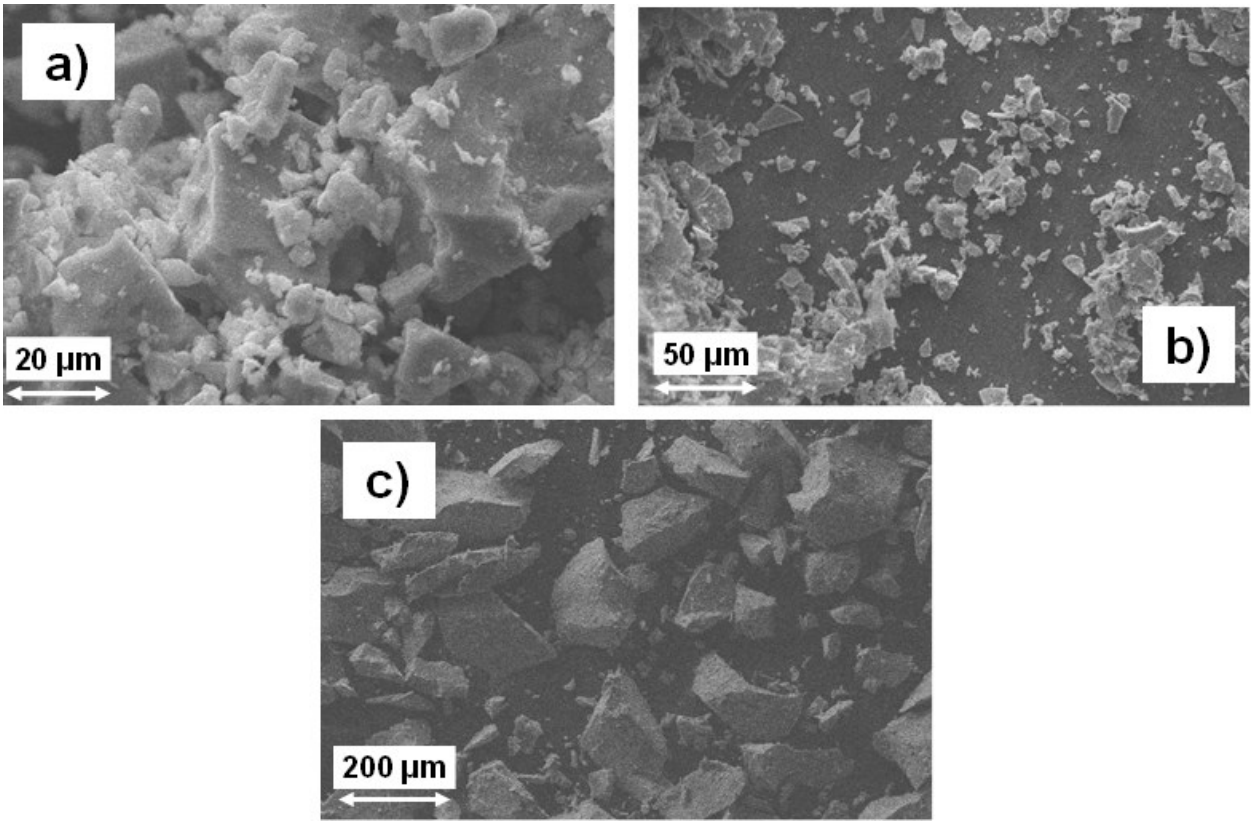


**Figure 3.5: SEM images of the a) 10, b) 44, and c) 420 μm particle size Mn reagents, as purchased. Images show the reagents have a highly irregular and undependable shape.**

the system is settling toward an equilibrium conversion, but the reaction *is* proceeding under kinetic limitations. Compare that result with both b) and c) in Figure 3.3. The equilibrium conversion for the 10 μm Mn particles is somewhat lower at the higher temperatures. Equilibrium conversion did occur faster in the smaller particles, and in the particle regimes evaluated for the present work, the Mn reached its equilibrium conversion faster with increased temperature. An interesting idea here is that it may be possible to combine both the smaller particles and lower temperatures to achieve a higher Mn conversion even a lower temperatures than would normally be considered kinetically favorable.

The images in Figure 3.5 of the 3 Mn particle regimes were acquired from a Zeiss (EVO MA 10) scanning electron microscope, with the goal of verifying the actual particle size of the reactants and to evaluate the particle geometry in order to apply solid-gas kinetic analyses such as the shrinking core model.[91] The irregular geometric nature of the particles adds some additional difficulty in applying a common kinetic model to the Mn-nitridation reaction system as many models make assumptions based on the solid particle geometry (sphere, long cylinder, flat plate, and more).[92] Additionally the mesh size specifications (-325 mesh and -40 mesh for the "44 μm and 420 μm" Mn particles should be taken as only a rough guide as the maximum particle size. The real distribution of particles will be measurably smaller than this value, according to Figure 3.5.

### 3.3.2 Jander's Unreacted Core Model

Jander's reaction rate law, eq (12), eq (13), and Figure 3.6, has successfully characterized solid-gas reactions kinetically controlled by a gaseous reactant diffusing through a solid product shell.[93] It is presented here in both differential and integral form to kinetically describe the nitridation of Mn powder:

$$\frac{dY_{Nitride}}{dt} = k_J \frac{3(1-Y_{Nitride})^{\frac{2}{3}}}{2\left[1-(1-Y_{Nitride})^{\frac{1}{3}}\right]} \tag{12}$$

$$k_J t = \left[1-(1-Y_{Nitride})^{\frac{1}{3}}\right]^2 \tag{13}$$

Where $k_J$ is Jander's rate constant ($min^{-1}$) and t is the reaction time (min).

Figure 3.7 shows the molar yield of $Mn_4N$ and $Mn_6N_{2.58}$ at 600 and 800 °C plotted along with Jander's unreacted core kinetic model. At 600 °C the reaction rate is slow enough that after 4 hours negligible $Mn_6N_{2.58}$ is present while at 800 °C both the 10 and 44 μm particle sizes react sufficiently fast such that $Mn_6N_{2.58}$ is the principal product after only 2 hours. At 800 °C, Mn is converted to the maximum amount of $Mn_4N$ in the first 5 min regardless of particle size. However, further nitridation to $Mn_6N_{2.58}$ is inhibited perhaps because nitrogen must diffuse through the product shell to react.

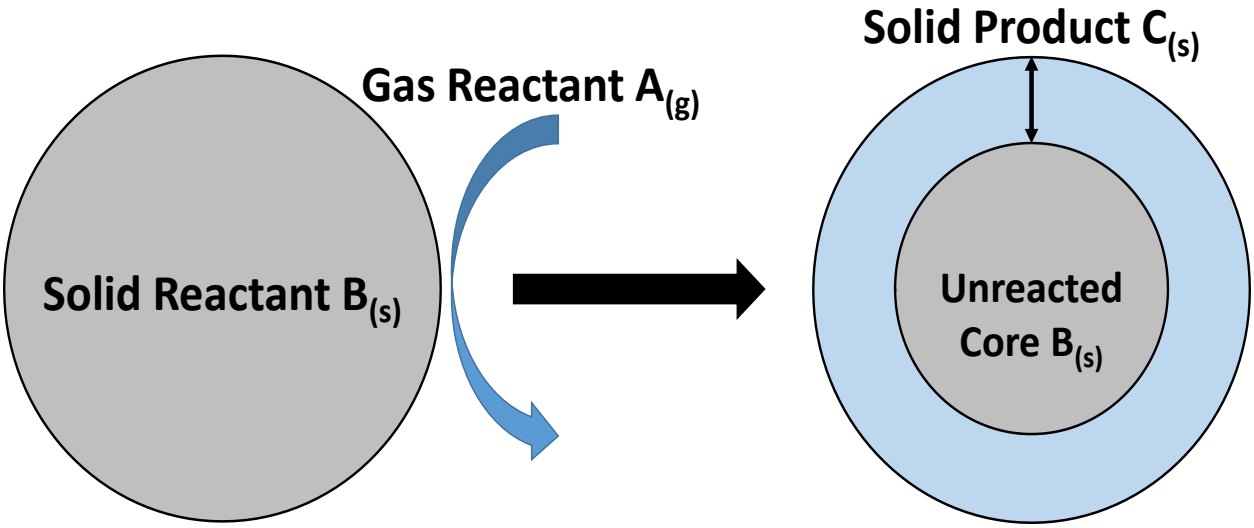


**Figure 3.6: Schematic for the generic unreacted core model. Including Jander's rate law in Eqs (12) and (13). Gas A and solid B react whereby a solid product shell C forms through which A must diffuse for the reaction to proceed.**

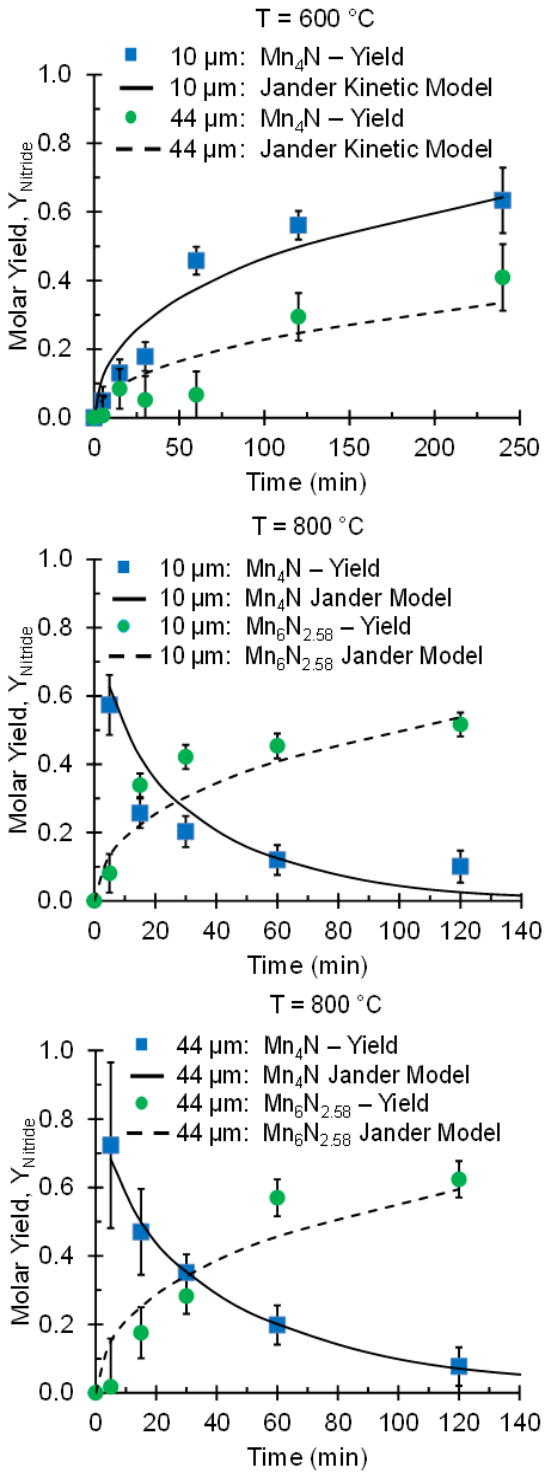


**Figure 3.7: Results of Applying Jander's Rate Law to Mn-nitridation at 600 and 800 °C for both 10 and 44 µm particle sizes. Error bars are from error propagation. The error on the abscissa is estimated at ± 2 min.**

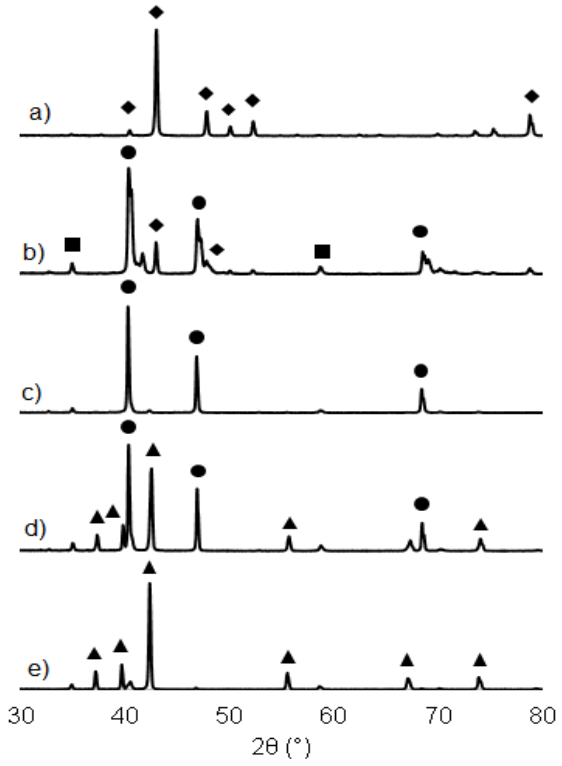


**Figure 3.8: Powder XRD of nitridation of a) 10 µm Mn at 700 °C for b) 5, c) 30, d) 120, and e) 240 min. The major peaks of each spectrum are: (●)$Mn_4N$ (ICDD PDF No. 01-089-4804), (▲)$Mn_6N_{2.58}$ (ICDD PDF No. 01-071-0200), (■) MnO (ICDD PDF No. 01-078-0424), and (♦) Mn (ICDD PDF No. 00-032-0637).**

Figure 3.8 shows the powder x-ray diffraction (XRD) spectra for the 10 µm Mn reactant after nitridation at 5, 30, 120, and 240 min together with the Mn sample as purchased. After 5 min the Mn peaks are almost all replaced by $Mn_4N$ peaks. The disappearance of the $Mn_4N$ peaks and replacement by $Mn_6N_{2.58}$ is also observable between 30 and 240 min.

Jander's unreacted core model, which considers diffusion of gaseous reactant through the product shell as the rate-limiting step, appears to characterize Mn-nitridation kinetics reasonably well as shown in Table 3.1. Correlation coefficients and rms errors[60] are used to describe the reasonableness of the application of the unreacted core model to the manganese-nitrogen system. Note that the goodness-of-fit of a solid-gas kinetic model should not be considered proof that the reaction proceeds under all of the assumptions used by the model.[92] Additionally, the assumption of spherical geometry is paramount in the realization of Jander's model. However, the SEM images in Figure 3.5 clearly show irregularly shaped particles. More work is required in order to prove that the reaction is truly solid-diffusion limited. Nevertheless, Jander's model empirically describes the system relatively well.

**Table 3.1: Reaction kinetics for Jander's unreacted core model applied to Mn-nitridation at atmospheric pressure. Estimated uncertainties are from error propagation.**

| Particle Size | Temp. | Chemical Product | Time Range | $k_J$ | $r_0$ | $R^2$ | rms |
|---|---|---|---|---|---|---|---|
| (μm) | (°C) | -- | (min) | ($min^{-1}$) | (mol N $mol^{-1}$ Mn $min^{-1}$) | -- | -- |
| 10 | 600 | $Mn_4N$ | 0 - 240 | (3.5 ± 0.5) X $10^{-4}$ | (1.0 ± 0.9) X $10^{-2}$ | 0.968 | 0.071 |
| | 700 | $Mn_4N$ | 0 - 30 | (2.5 ± 0.4) X $10^{-3}$ | (6.3 ± 0.9) X $10^{-2}$ | 0.992 | 0.019 |
| | | $Mn_4N$ | 30 - 240 | (1.1 ± 0.3) X $10^{-3}$ | -(4.6 ± 3.9) X $10^{-3}$ | 0.994 | 0.052 |
| | | $Mn_6N_{2.58}$ | 30 - 240 | (1.4 ± 1.2) X $10^{-3}$ | (1.0 ± 0.7) X $10^{-2}$ | 0.999 | 0.123 |
| | 800 | $Mn_4N$ | 5 - 120 | (4.2 ± 1.1) X $10^{-3}$ | -(3.2 ± 1.3) X $10^{-2}$ | 0.940 | 0.076 |
| | | $Mn_6N_{2.58}$ | 0 - 120 | (4.3 ± 0.7) X $10^{-3}$ | (1.6 ± 1.3) X $10^{-2}$ | 0.890 | 0.068 |
| < 44 | 600 | $Mn_4N$ | 0 - 240 | (6.0 ± 6.0) X $10^{-5}$ | (1.4 ± 1.2) X $10^{-3}$ | 0.996 | 0.038 |
| | 700 | $Mn_4N$ | 0 - 60 | (1.1 ± 0.3) X $10^{-3}$ | (4.6 ± 0.5) X $10^{-2}$ | 0.987 | 0.035 |
| | | $Mn_4N$ | 60 - 240 | (4.1 ± 0.2) X $10^{-4}$ | -(1.1 ± 2.1) X $10^{-3}$ | 0.982 | 0.027 |
| | | $Mn_6N_{2.58}$ | 30 - 240 | (5.7 ± 5.5) X $10^{-4}$ | (3.5 ± 3.0) X $10^{-3}$ | 0.960 | 0.082 |
| | 800 | $Mn_4N$ | 5 - 120 | (2.5 ± 2.4) X $10^{-3}$ | -(2.5 ± 2.4) X $10^{-2}$ | 0.996 | 0.022 |
| | | $Mn_6N_{2.58}$ | 0 - 120 | (4.1 ± 0.6) X $10^{-2}$ | (3.5 ± 3.4) X $10^{-2}$ | 0.960 | 0.082 |

Comparing the same reaction temperatures and times across Table 3.1 it is clear that the smaller particle size exhibits larger rate constants, $k_J$, and initial rates, $r_0$. This makes sense as

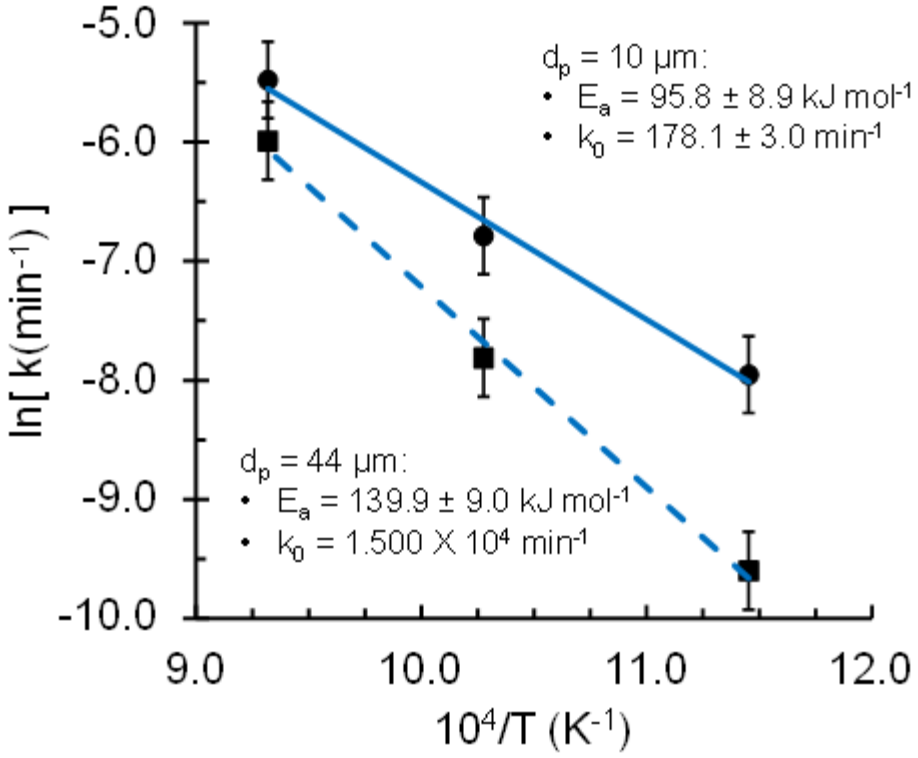


**Figure 3.9: Arrhenius plot for the $Mn_4N$ yields of the 10 and 44 µm Mn reactant particle sizes. ● and ■ represent the 10 and 44 µm sizes respectively. The solid and dashed blue lines are the best-fit according to eq (15). Estimated uncertainties are from error propagation. Error on the abscissa is estimated at ± 0.1 $K^{-1}$.**

more surface area is immediately available to the reactant gas and/or the nitrogen diffusion path is reduced. However Table 3.1 and Figure 3.9 encourage use of a particle size smaller than 10 µm. Above 700 °C the difference in time required to approach equilibrium conversion is very similar between the 2 particle sizes. Reducing the particle size further can encourage greater nitrogen uptake at lower temperatures where equilibrium conversion is less inhibited.

### 3.3.3 Arrhenius Relationship

Activation energies ($E_a$, kJ $mol^{-1}$) are calculated by exploiting the temperature dependence of rate constants known as the Arrhenius[94] eq:

$$k_J(T) = k_0 e^{\frac{E_a}{RT}} \tag{14}$$

$$ln|k_J(T)| = ln|k_0| - \frac{E_a}{R}\left(\frac{1}{T}\right) \tag{15}$$

Where $k_0$ is the pre-exponential factor ($min^{-1}$), R is the universal gas constant, and T is the absolute temperature. Taking the natural logarithm of eq (14) yields eq (15) which allows a solution for $E_a$ and $k_0$ by plotting $ln[k_J]$ vs. 1/T. The Arrhenius plot for $Mn_4N$ yields for both the 10 and 44 μm samples is shown in Figure 3.9 along with the calculated activation energies and pre-exponential factors. The smaller particle size does have a smaller apparent activation energy by 44.1 kJ $mol^{-1}$. This makes sense as more Mn is available to react immediately upon heating with the reactant gas.

## 3.4 Conclusion

An investigation was performed on the nitridation of manganese by atmospheric $N_2$ at elevated temperature on Mn particle sizes of 10 and 44 μm. Establishing quantifiable and predictable behavior for the nitridation step of the $NH_3$ synthesis cycle is paramount to the broader efficacy of the overall process.

Isothermal nitrogen fixation furnace experiments confirmed that equilibrium nitrogen concentration in Mn decreases as reaction temperature increases. Jander's unreacted core kinetic model mathematically described Mn nitridation relatively well. However, while Jander's rate law does assume that a gaseous reactant diffusing through the solid product layer is the rate limiting step, not enough information is provided to confirm this assumption specifically applies to the system in question.

While rate constants and initial rates were as much as an order of magnitude larger for nitridation of the 10 μm particles, it is clear that even smaller particles will further improve reactant performance. Specifically, the goal is to achieve the higher reaction rate that occurs at or above 800 °C without sacrificing the reduced equilibrium nitrogen concentration. The Arrhenius equation was used to determine the activation energies for nitridation of 10 and 44 μm particles by

exploiting the temperature-dependence of the reaction rate constant. As expected the $E_a$ of the 10 μm Mn reactant was lower than that of the 44 μm Mn as the (potential) diffusion path is decreased and the available surface area of reaction is increased.

# Chapter 4 - Conclusions

More $NH_3$ is necessary to allow global population to exceed 9.6 billion by 2050. However it is incumbent upon us to develop a process which contributes less to the overall carbon footprint of food production. The solar cycle envisioned in this work shows promise as a vector toward sustainable $NH_3$ synthesis. Not to compete with Haber-Bosch but instead to supplement that process by reaching those whom it does not reach.

A thermochemical cycle was presented where the hydrogen from steam was reacted with Mn-nitride to produce $NH_3$ and MnO. The MnO was then subsequently reduced in a dilute $CH_4/N_2$ gas stream to reproduce the nitride. Manganese readily fixes nitrogen, quickly and efficiently. However a Na-promotor was required to be added to the nitride in order to yield $NH_3$. The resulting MnO partially reduced with under great care.

Jander's reaction rate law was used to model the kinetics of Mn for both 10 μm and < 44 μm particle sizes. However inspection under SEM showed the particles were not remotely spherical as assumed in the derivation of the rate law. The apparent activation energy was lower by 44.1 kJ $mol^{-1}$ for the smaller particle size Mn. Reducing the particle size further will allow greater Mn conversion at lower temperature.

It is apparent the relative stability of metal oxides over metal nitrides is a significant hurdle to overcome. If in a particular chemistry of alternating metal reactions with nitrogen and oxygen, the oxide is always more stable than the nitride. That is, recovering the zero-oxidation state metal from the oxide will be more difficult if that same metal readily formed the nitride. It is just as true in reverse that a metal oxide when easy to reduce to the metal, will not form a stable nitride upon nitridation. A similar relationship also exists for the $NH_3$ synthesis and oxide reduction reactions.

See appendix B for more a review of the thermodynamics and how an open system can aid in mitigating some of these challenges.

# Chapter 5 - Future Work

In addition the use of open systems, alloying materials may promote desired reactions. The research the Mn-Ni and Mn-Fe alloys should be continued. It will be very interesting to see how the addition of another transition metal will promote the reaction. This is comparable to the promoted-Fe catalyst used in the HB process. I also think that using group 1 metals would be something worth trying as promotors (similar to the NaOH used in chapter 2). However, the zero-oxidation state metal should be used instead of an oxide version. The oxygen from the NaOH was present as $\alpha$-$NaMnO_2$ after the reaction – and Mn-oxides are not trivial to reduce. The work shown here and additional work indicates alkali metals would be efficacious in promoting the $NH_3$ synthesis reaction and may also aid cycling.

A future student may find it beneficial to work on finding a more efficient way to present the metal particles to the reacting gas. A porous support would greatly increase the surface area available for chemical reaction, as in heterogeneous catalysis, and may improve overall conversions and yields.

It seems that heroic measures are required in order to significantly limit the amount of $O_2/H_2O$ in the system which then contacts the Mn forming the oxide – and Mn-oxides are not trivial to reduce. This is a step that is necessary to improve the quantification of nitrogen fixed to the metal and the nitrogen which leaves the metal (upon reaction with gaseous $H_2$ for $NH_3$ formation, showing a mass loss instead of gain, not shown in this dissertation). Preventing the formation of metal oxides provides an additional degree of freedom and the mass added of nitrogen is then just the mass after the reaction minus the mass of the zero-oxidation state metal before the reaction. Quantification of nitrogen is further discussed in appendix C.3.

Bulk work with nanoparticles: The possibilities that accompany moving to nanoscale materials are really interesting. The problem is that nano-metals are extremely reactive in air. Heroic efforts are required just to work with these materials relative to what we are already doing. Furthermore, we still need to find a way to create enough nanoparticles such that we aren't creating $NH_3$ at the nanoscale also. We want to use the reactivity and energetics of nanoparticles to make bulk $NH_3$.

The project as a whole is moving away from classical chemical engineering and toward materials science. I am extremely encouraged that the work with Dr. Liu's group is yielding some tangible guidance as to how to proceed in terms of cycled material. I reflect on just how much trial-and-error went in to developing better $NH_3$ synthesis catalysts for HB. Yet all modern HB plants use the promoted-Fe catalyst developed by Mittasch around a century ago. We need to find a way to use the computational techniques at our disposal to guide the experimentation.

# Chapter 6 - References


1. Smil, V. Detonator of the Population Explosion. *Nature* **1999**, *400*, 415.
2. Newton, W. E. Nitrogen Fixation. In *Encyclopedia of Agrochemicals;* Plimmer, J.R., Gammon, D.W., Ragsdale, N.A., Eds.; Wiley: New York, 2003.
3. Housecroft, C. E.; Sharpe, A. G. *Inorganic Chemistry;* Pearson: New York, 2012.
4. Smil, V. Population Growth and Nitrogen: An Exploration of a Critical Existential Link. *Population and Development Review* **1991**, *17*, 569-601.
5. Borlaug, N. E. In *The Green Revolution, Peace, and Humanity,* Awarding of the 1970 Nobel Peace Prize, Oslo, Norway, Dec 11, 1970; Nobelprize.org. Nobel Media AB 2014. http://www.nobelprize.org/nobel_prizes/peace/laureates/1970/borlaug-lecture.html (accessed March 18, 2018).
6. Smil, V. Nitrogen and Food Production: Proteins for Human Diets. *Ambio* **2002**, *31*, 126-131.
7. Smil, V. *Enriching the Earth: Fritz Haber, Carl Bosch, and the Transformation of World Agriculture;* MIT Press: Cambridge, MA, 2001.
8. Nobel Media AB 2014. The Nobel Prize in Chemistry 1918. http://www.nobelprize.org/nobel_prizes/chemistry/laureates/1918 (accessed June 16, 2015).
9. Nobel Media AB 2014. The Nobel Prize in Chemistry 1931. http://www.nobelprize.org/nobel_prizes/chemistry/laureates/1931/ (accessed June 16, 2015).
10. Howarth, R. W. Coastal Nitrogen Pollution: A Review of Sources and Trends Globally and Regionally. *Harmful Algae* **2008**, *8*, 14-20.
11. Department of Economic and Social Affairs, Population Division. *World Population Prospects: The 2017 Revision;* 2017. United Nations Web Site https://esa.un.org/unpd/wpp/Download/Standard/Population/ (accessed March 18, 2018).
12. Department of Economic and Social Affairs, Population Division. *The World at Six Billion;* Report ESA/P/WP.154; 1999. United Nations Web Site http://www.un.org/esa/population/publications/sixbillion/sixbillion.htm (accessed March 18, 2018).
13. IFA. World Nitrogen Fertililzer Consumption, 2017. International Fertilizer Association. http://ifadata.fertilizer.org/ucSearch.aspx (accessed March 18, 2018).

14. Centre for Industry Education Collaboration. Ammonia, 2016. The Essential Chemical Industry - Online. http://www.essentialchemicalindustry.org/chemicals/ammonia.html (accessed March 23, 2018).
15. Apodaca, L. E. Nitrogen (Fixed)-Ammonia. *U.S. Geological Survey, Mineral Commodity Summaries* **2018**, 116-117.
16. Foley, J. A Five-Step Plan to Feed the World. *National Geographic* **2014***, 225*, 27-57.
17. Pfromm, P. H. Towards sustainable agriculture: Fossil-free ammonia. *Journal of Renewable and Sustainable Energy.* **2017**, 9, 034702.
18. Slack, A. V.; James, G. R. *Ammonia, Part III;* Marcel Dekker: New York, 1977.
19. Eggeman, T. Ammonia. *Kirk-Othmer Encyclopedia of Chemical Technology,* 5th ed.; Wiley: New York, 2010; Vol. 2, pp 678-710.
20. Kirova-Yordanova, Z. Exergy Analysis of Industrial Ammonia Synthesis. *Energy* **2004***, 29*, 2373-2384.
21. ThyssenKrupp Uhde. Ammonia, 2011. ThyssenKrupp Industrial Solutions. http://www.thyssenkrupp-industrial-solutions.com/fileadmin/documents/brochures/uhde_brochures_pdf_en_5.pdf (accessed Nov 8, 2016).
22. Rafiqul, I.; Weber, C.; Lehmann, B.; Voss, A. Energy Efficiency Improvements in Ammonia Production-Perspectives and Uncertainties. *Energy* **2005***, 30*, 2487-2504.
23. Noelker, K.; Ruether, J. Low Energy Consumption Ammonia Production: Baseline Energy Consumption, Options for Energy Optimization. Presented at the Nitrogen + Syngas Conference [online], Duesseldorf, Feb 21-24, 2011. Thyssenkrupp Industrial Solution Web site. https://www.thyssenkrupp-industrial-solutions.com/media/products_services/fertilizer_plants/ammonium_sulphate_plants/low_energy_consumption_ammonia_production_2011_paper.pdf (accessed March 23, 2018).
24. Ritter, S. K. The Haber-Bosch Reaction: An Early Chemical Impact on Sustainability. *Chem. Eng. News* **2008***, 86*.
25. IPCC. Climate Change 2007: Mitigation. Contribution of Working Group III to the Fourth Assessment Report of the Intergovernmental Panel on Climate Change [Online]; Metz, B., Davidson, O.R., Bosch, P.R., Dave, R., Meyer, L.A., Eds.; Cambridge University Press: New

York, 2007; https://www.ipcc.ch/pdf/assessment-report/ar4/wg3/ar4_wg3_full_report.pdf (accessed March 23, 2018).

26. Lippmann, D.; Larsen, J. Uhde dual-pressure process for large-scale ammonia plants, 2004. ThyssenKrupp Web site: https://www.thyssenkrupp.com/documents/Publikationen/Techforum/techforum_e_7_2004.pdf (accessed Nov 8, 2016).
27. Michalsky, R.; Parman, B. J.; Amanor-Boadu, V.; Pfromm, P. H. Solar thermochemical production of ammonia from water, air and sunlight: Thermodynamic and economic analysis. *Energy* **2012**, *42*, 251-260.
28. Silberberg, M. S. *Principles of General Chemistry;* McGraw-Hill: New York, 2007.
29. Mittasch, A.; Fankenburg, W. Early Studies of Multicomponent Catalysts. In *Advances in Catalysis*; Frankenburg, W.G., Komarewsky, V.I., Rideal, E.K., Ed.; Academic Press: New York, 1950; Vol. 2, pp 81-104.
30. Jacobsen, C. J. H.; Dahl, S.; Clausen, B. S.; Bahn, S.; Logadottir, A.; Nørskov, J. K. Catalyst Design by Interpolation in the Periodic Table: Bimetallic Ammonia Synthesis Catalysts. *J. Am. Chem. Soc.* **2001**, *123*, 8404-8405.
31. Schlögl, R. Catalytic Synthesis of Ammonia - A "Never Ending Story"? *Angew. Chem. Int. Ed.* **2003**, *42*, 2004-2008.
32. IFA. Fertilizers, Climate Change, and Enhancing Agricultural Productivity Sustainably, 2009. International Fertilizer Association. https://www.fertilizer.org/images/Library_Downloads/2009_ifa_climate_change.pdf (accessed March 24, 2018).
33. Amar, I. A.; Lan, R.; Petit, C.; Tao, S. Solid-state electrochemical synthesis of ammonia: a review. *J. Solid State Electrochem.* **2011**, *15*, 1845-1860.
34. Valov, I.; Luerssen, B.; Mutoro, E.; Gregoratti, L.; De Souza, R. A.; Bredow, T.; Günther, S.; Barinov, A.; Dudin, P.; Martin, M.; Janek, J. Electrochemical activation of molecular nitrogen at the Ir/YSZ interface. *Phys. Chem. Chem. Phys.* **2011**, *13*, 3394-3410.
35. Lee, D.; Fischer, C. C.; Valov, I.; Reinacher, J.; Stork, A.; Lerch, M.; Janek, J. An EMF cell with a nitrogen solid electrolyte-on the transference of nitrogen ions in yttria-stabilized zirconia. *Phys. Chem. Chem. Phys.* **2011**, *13*, 1239-1242.

36. Lerch, M.; Janek, J.; Becker, K. D.; Berendts, S.; Boysen, H.; Bredow, T.; Dronskowski, R.; Ebbinghaus, S. G.; Kilo, M.; Lumey, M. W.; Martin, M.; Reimann, C.; Schweda, E.; Valov, I.; Wiemhofer, H. D. Oxide Nitrides: From Oxides to Solids with Mobile Nitrogen Ions. *Prog. Solid State Chem.* **2009**, *37*, 81-131.

37. Kordali, V.; Kyriacou, G.; Lambrou, C. Electrochemical synthesis of ammonia at atmospheric pressure and low temperature in a solid polymer electrolyte cell. *Chem. Commun.* **2000**, *0*, 1673-1674.

38. Licht, S.; Cui, B.; Wang, B.; Li, F.; Lau, J.; Liu, S. Ammonia Synthesis by $N_2$ and Steam Electrolysis in Molten Hydroxide Suspensions of Nanoscale $Fe_2O_3$. *Science* **2014**, *345*, 637-640.

39. Skodra, A.; Stoukides, M. Electrocatalytic Synthesis of Ammonia from Steam and Nitrogen at Atmospheric Pressure. *Solid State Ionics* **2009**, *180*, 1332-1336.

40. Giddey, S.; Badwal, S. P. S.; Kulkarni, A. Review of electrochemical ammonia production technologies and materials. *Int. J. Hydrogen Energy* **2013**, *38*, 14576-14594.

41. Fryzuk, M. D. Side-on End-on Bound Dinitrogen - An Activated Bonding Mode That Facilitates Functionalizing Molecular Nitrogen. *Acc. Chem. Res.* **2009**, *42*, 127-133.

42. Gilbertson, J. D.; Szymczak, N. K.; Tyler, D. R. Reduction of $N_2$ to Ammonia and Hydrazine Utilizing $H_2$ as the Reductant. *J. Am. Chem. Soc.* **2005**, *127*, 10184-10185.

43. Knobloch, D. J.; Lobkovsky, E.; Chirik, P. J. Dinitrogen Cleavage and Functionalization by Carbon Monoxide Promoted by a Hafnium Complex. *Nature Chemistry* **2010**, *2*, 30-35.

44. Rodriguez, M. M.; Bill, E.; Brennessel, W. W.; Holland, P. L. $N_2$ Reduction and Hydrogenation to Ammonia by a Molecular Iron-Potassium Complex. *Science* **2011**, *334*, 780-783.

45. Khaselev, O.; Turner, J. A. A Monolithic Photovoltaic-Photoelectrochemical Device for Hydrogen Production via Water Splitting. *Science* **1998**, *280*, 425-427.

46. Heidlage, M. G.; Kezar, E. A.; Snow, K. C.; Pfromm, P. H. Thermochemical Synthesis of Ammonia and Syngas from Natural Gas at Atmospheric Pressure. *Ind. Eng. Chem. Res.* **2017**, *56*, 14014-14024.

47. Michalsky, R.; Pfromm, P. H. An Ionicity Rationale to Design Solid Phase Metal Nitride Reactants for Solar Ammonia Production. *J. Phys. Chem. C* **2012**, *116*, 23243-23251.

48. Chamberlin, J.; Jayne, T. S.; Headey, D. Scarcity Amidst Abundance? Reassessing the Potential for Cropland Expansion in Africa. *Food Policy* **2014**, *48*, 51-65.

49. Lunge, G. *Coal-Tar and Ammonia;* Gurney and Jackson: London, 1916.
50. Maxted, E. B. *Ammonia and the Nitrides: With Special Reference to Their Synthesis;* J. & A. Churchill: London, 1921.
51. Sauchelli, V. *Fertilizer Nitrogen: Its Chemistry and Technology;* Reinhold: New York, 1964.
52. Michalsky, R.; Pfromm, P. H. Chromium as Reactant for Solar Thermochemical Synthesis of Ammonia from Steam, Nitrogen, and Biomass at Atmospheric Pressure. *Solar Energy* **2011***, 85*, 2642-2654.
53. Apodaca, L. E. Nitrogen (Fixed)-Ammonia. *U.S. Geological Survey, Mineral Commodity Summaries* **2016**, 118-119.
54. Pool, J. A.; Lobkovsky, E.; Chirik, P. J. Hydrogenation and Cleavage of Dinitrogen to Ammonia with a Zirconium Complex. *Nature* **2004***, 427*, 527-530.
55. Badische Anilin- und Sodafabriken (BASF). Verfahren zur synthetischen Darstellung von Ammoniak aus seinen Elementen. Deutsches Reichspatent 235 421, October 13, **1908**.
56. Abghoui, Y.; Garden, A. L.; Hlynsson, V. F.; Bjorgvinsdottir, S.; Olafsdottir, H.; Skulason, E. Enabling Electrochemical Reduction of Nitrogen to Ammonia at Ambient Conditions Through Rational Catalyst Design. *Phys. Chem. Chem. Phys.* **2015***, 17*, 4909-4918.
57. Yandulov, D. V.; Schrock, R. R. Catalytic Reduction of Dinitrogen to Ammonia at a Single Molybdenum Center. *Science* **2003***, 301*, 76-78.
58. Haber, F.; van Oordt, G. Über die Bildung von Ammoniak aus den Elementen. *Zeitschrift für Anorganische und Allgemeine Chemie* **1905***, 44*, 341-378.
59. Gálvez, M. E.; Halmann, M.; Steinfeld, A. Ammonia Production via a Two-Step $Al_2O_3$/AlN Thermochemical Cycle. 1. Thermodynamic, Environmental, and Economic Analyses. *Ind. Eng. Chem. Res.* **2007***, 46*, 2042-2046.
60. Gálvez, M. E.; Frei, A.; Halmann, M.; Steinfeld, A. Ammonia Production via a Two-Step $Al_2O_3$/AlN Thermochemical Cycle. 2. Kinetic Analysis. *Ind. Eng. Chem. Res.* **2007***, 46*, 2047-2053.
61. Gálvez, M. E.; Hischier, I.; Frei, A.; Steinfeld, A. Ammonia Production via a Two-Step $Al_2O_3$/AlN Thermochemical Cycle. 3. Influence of the Carbon Reducing Agent and Cyclability. *Ind. Eng. Chem. Res.* **2008***, 47*, 2231-2237.

62. Gálvez, M. E.; Frei, A.; Meier, F.; Steinfeld, A. Production of AlN by Carbothermal and Methanothermal Reduction of $Al_2O_3$ in a $N_2$ Flow Using Concentrated Solar Radiation. *Ind. Eng. Chem. Res.* **2009**, *48*, 528-533.
63. Steinfeld, A.; Larson, C.; Palumbo, R.; Foley, M. Thermodynamic Analysis of the Co-Production of Zinc and Synthesis Gas Using Solar Process Heat. *Energy* **1996**, *21*, 205-222.
64. Kodama, T. High-Temperature Solar Chemistry for Converting Solar Heat to Chemical Fuels. *Prog. Energy Combust. Sci.* **2003**, *29*, 567-597.
65. Steinfeld, A.; Weimer, A. W. Thermochemical Production of Fuels with Concentrated Solar Energy. *Opt. Express* **2010**, *18*, A100-A111.
66. Michalsky, R.; Pfromm, P. H. Thermodynamics of Metal Reactants for Ammonia Synthesis from Steam, Nitrogen, and Biomass at Atmospheric Pressure. *AIChE J.* **2012**, *58*, 3203-3213.
67. Jacoby, M. Rechargeable Metal-Air Batteries. *Chem. Eng. News* **2010**, *88*, 29-31.
68. Cairns, A. G.; Gallagher, J. G.; Hargreaves, J. S. J.; Mckay, D.; Rico, J. L.; Wilson, K. The Effect of Low Levels of Dopants upon the Formation and Properties of Beta-Phase Molybdenum Nitride. *J. Solid State Chem.* **2010**, *183*, 613-619.
69. Miller, J. E.; Allendorf, M. D.; Diver, R. B.; Evans, L. R.; Siegel, N. P.; Stuecker, J. N. Metal Oxide Composites and Structures for Ultra-High Temperature Solar Thermochemical Cycles. *J. Mater. Sci.* **2008**, *43*, 4714-4728.
70. Roeb, M.; Muller-Steinhagen, H. Concentrating on Solar Electricity and Fuels. *Science* **2010**, *329*, 773-774.
71. Barin, I.; Knacke, O.; Kubaschewski, O. *Thermochemical Properties of Inorganic Substances;* Springer: New York, 1973.
72. Barin, I.; Knacke, O.; Kubaschewski, O. *Thermochemical Properties of Inorganic Substances - Supplement;* Springer: New York, 1977.
73. Perry, R. H.; Green, D. W.; Maloney, J. O. *Perry's Chemical Engineers' Handbook;* McGraw-Hill: New York, 1997.
74. Galadima, A.; Muraza, O. From Synthesis Gas Production to Methanol Synthesis and Potential Upgrade to Gasoline Range Hydrocarbons: A Review. *Journal of Natural Gas Science and Engineering* **2015**, *25*, 303-316.

75. Lillebo, A. H.; Holmen, A.; Enger, B. C.; Blekkan, E. A. Fischer-Tropsch Conversion of Biomass-Derived Synthesis Gas to Liquid Fuels. *Wiley Interdisciplinary Reviews - Energy and Environment* **2013**, *2*, 507-524.

76. Khodakov, A. Y.; Chu, W.; Fongarland, P. Advances in the Development of Novel Cobalt Fischer-Tropsch Catalysts for Synthesis of Long-Chain Hydrocarbons and Clean Fuels. *Chem. Rev.* **2007**, *107*, 1692-1744.

77. Michalsky, R.; Pfromm, P. H. Thermochemical Ammonia and Hydrocarbons. U.S. Pat. Appl. 2015/0315032 A1, Nov 5, 2015.

78. ICDD. The Internal Centre for Diffraction Data Home Page. http://www.icdd.com/index.htm (accessed Nov 7, 2017).

79. Geankoplis, C. J. *Transport Processes and Separation Process Principles;* Prentice Hall: Upper Saddle River, 2009.

80. Brunauer, S.; Emmett, P. H.; Teller, E. Adsorption of Gases in Multimolecular Layers. *J. Amer. Chem. Soc.* **1938**, *60*, 309-319.

81. Lowell, S.; Shields, J. E.; Thomas, M. A.; Thommes, M. *Characterization of Porous Solids and Powders: Surface Area, Pore Size and Density;* Springer: Dordrecht, 2006.

82. Bird, R. B.; Stewart, W. E.; Lightfoot, E. N. *Transport Phenomena*; Wiley: New York, 2007; pp 517-519.

83. Michalsky, R.; Pfromm, P. H.; Steinfeld, A. Rational Design of Metal Nitride Redox Materials for Solar-Driven Ammonia Synthesis. *Interface Focus* **2015**, *5*.

84. Qiu, C.; Guillermet, A. F. Predicative Approach to the Entropy of Manganese Nitrides and Calculation of the Mn-N Phase Diagram. *Z. MetaIlkd.* **1993**, *84*, 11-22.

85. Felder, R. M.; Rousseau, R. W. *Elementary Principles of Chemical Processes;* Wiley: Hoboken, 2005; pp 123, 135.

86. Knacke, O.; Kubaschewski, O.; Hesselmann, K. *Thermochemical Properties of Inorganic Substances;* Springer-Verlag: New York, 1991; Vol. I, II.

87. Anacleto, N.; Ostrovski, O.; Ganguly, S. Reduction of Manganese Oxides by Methane-Containing Gas. *ISIJ Int.* **2004**, *44*, 1480-1487.

88. Kemmitt, R. D. W.; Peacock, R. D. *The Chemistry of Manganese, Technetium, and Rhenium;* Pergamon Press: Oxford, 1975.

89. Gokcen, N. A. The Mn-N (Manganese-Nitrogen) System. *Bulletin of Alloy Phase Diagrams* **1990**, *11*, 33-42.

90. Bale, C. W.; Bèlisle, E. Fact-Web Suite of Interactive Programs. http://www.factsage.com (accessed Jan 25, 2016).

91. Levenspiel, O. *Chemical Reaction Engineering;* Wiley: New York, 1999.

92. AnonymousSzekely, J.;Evans, J.W.;Sohn, H.Y. *Gas-Solid Reactions;* Academic Press, New York, 1976.

93. Shimizu, A.; Hao, Y. Influence of Particle Contact on the Estimation of Powder Reaction Kinetics of Binary Mixtures. *J. Am. Ceram. Soc.* **1997**, *80*, 557-568.

94. Fogler, S. H. *Elements of Chemical Reaction Engineering;* Pearson Education, Inc.: Upper Saddle River, 2006.

95. Felder, R. M.; Rousseau, R. W. *Elementary Principles of Chemical Processes;* Wiley: Hoboken, 2005.

96. Smith, J. M.; Van Ness, H. C.; Abbott, M. M. *Introduction to Chemical Engineering Thermodynamics;* McGraw-Hill: New York, 2005; .

97. Pecharsky, V. K.; Zavalij, P. Y. *Fundamentals of Powder Diffraction and Structural Characterization of Materials;* Springer: New York, 2009.

98. Chung, F. H. Quantitative interpretation of x-ray patterns of mixtures. III. Simultaneous determination of a set of reference intensities. *J. Appl. Crystallogr.* **1975**, *8*, 17-19.

99. Connolly, J. R. *Introduction to Quantitative X-Ray Diffraction Methods;* Introduction to X-Ray Powder Diffraction: 2012.

100. Speakman, S. A. Basics of X-Ray Powder Diffraction, 2013. MIT Center for Materials Science and Engineering. http://prism.mit.edu/xray/oldsite/1%20Basics%20of%20X-Ray%20Powder%20Diffraction.pptx (accessed April 7, 2016).

101. Zhang, J. Z.; Xu, S.; Zhao, Y. P. Kinetics of nitrogen diffusion in granular manganese. *Journal of Iron and Steel Research International* **2008**, *15*, 85-88.

# Appendix A - Supplementary Material to Accompany Chapter 2

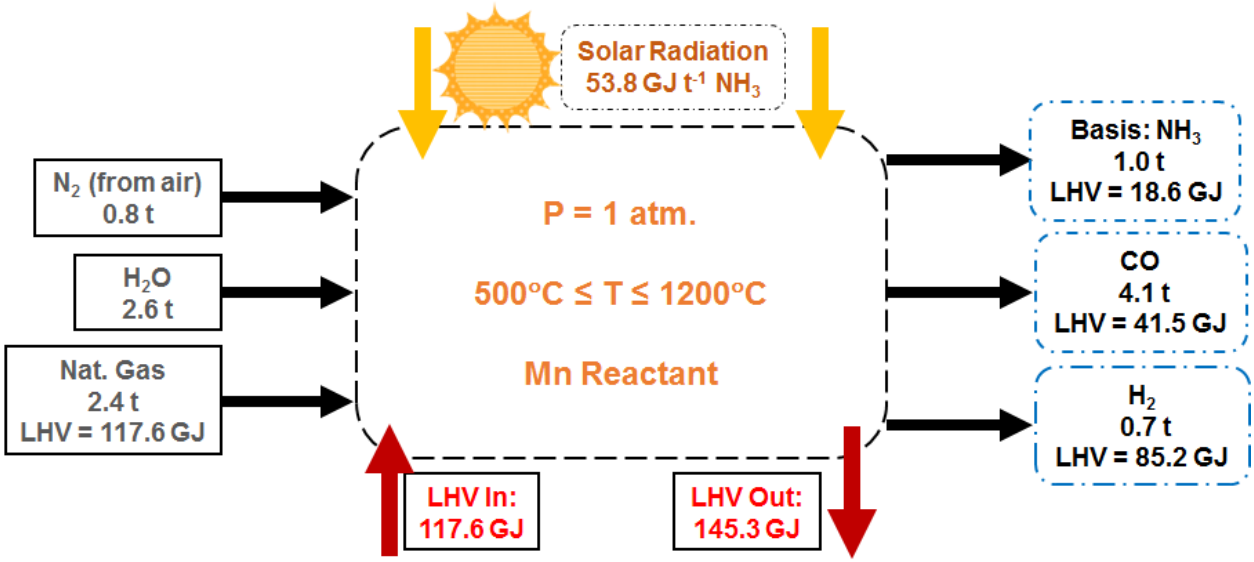


**A. 1: Reproduction of Figure 2.2. Simplified process diagram showing step-up in energy provided in syngas (CO and $H_2$) produced over the natural gas input. LHV is lower heating value[95] of reactants and products. Calculations are based on mass balances and reaction enthalpies (eqs 1-4 of A. 2) only. Solar radiation input is calculated solely from the energy required for the endothermic reduction reaction (eq 3). Energy required for input and exit gas conditioning and separation is neglected. Heat integration is also neglected.**

$$\frac{5}{2}Mn_{(s)} + \frac{1}{2}N_{2(g)} \leftrightarrow \frac{1}{2}Mn_5N_{2(s)} \quad (1)$$

$$\Delta H_{Rxn1}^{T=800°C} = -91.0\ kJ\ mol^{-1} \qquad \Delta G_{Rxn1}^{T=800°C} = -64.3\ kJ\ mol^{-1}$$

$$\frac{1}{2}Mn_5N_{2(s)} + \frac{5}{2}H_2O_{(g)} \leftrightarrow \frac{5}{2}MnO_{(s)} + NH_{3(g)} + H_{2(g)} \quad (2)$$

$$\Delta H_{Rxn2}^{T=500°C} = -302.4\ kJ\ mol^{-1} \qquad \Delta G_{Rxn2}^{T=500°C} = -230.5\ kJ\ mol^{-1}$$

$$\frac{5}{2}MnO_{(s)} + \frac{5}{2}CH_{4(g)} \leftrightarrow \frac{5}{2}Mn_{(s)} + \frac{5}{2}CO_{(g)} + 5H_{2(g)} \quad (3)$$

$$\Delta H_{Rxn3}^{T=1150°C} = 916\ kJ\ mol^{-1} \qquad \Delta G_{Rxn3}^{T=1150°C} = -57.1\ kJ\ mol^{-1}$$

$$\frac{1}{2}N_{2(g)} + \frac{5}{2}H_2O_{(g)} + \frac{5}{2}CH_{4(g)} \leftrightarrow NH_{3(g)} + \frac{5}{2}CO_{(g)} + 6H_{2(g)} \quad (4)$$

$$\Delta H_{Overall}^{T=25°C} = 469.3\ kJ\ mol^{-1}$$

**A. 2: Reproduction of chemical reactions (eqs 1 – 4). The reaction enthalpies and Gibbs energies were calculated from tabulated values.**

Mass Inputs

$N_2$:

| | | | | | | |
|---|---|---|---|---|---|---|
| 1 | 1000 | 1 | 0.5 | 28.014 | 1 | 0.82 |
| | 1 | 17.031 | 1 | 1 | 1000 | t $N_2$ |

| | | | | | |
|---|---|---|---|---|---|
| t $NH_3$ | kg $NH_3$ | kmol $NH_3$ | kmol $N_2$ | kg $N_2$ | t $N_2$ |
| | t $NH_3$ | kg $NH_3$ | kmol $NH_3$ | kmol $N_2$ | kg $N_2$ |

$H_2O$:

| | | | | | | |
|---|---|---|---|---|---|---|
| 1 | 1000 | 1 | 2.5 | 18.015 | 1 | 2.64 |
| | 1 | 17.031 | 1 | 1 | 1000 | t $H_2O$ |

| | | | | | |
|---|---|---|---|---|---|
| t $NH_3$ | kg $NH_3$ | kmol $NH_3$ | kmol $H_2O$ | kg $H_2O$ | t $H_2O$ |
| | t $NH_3$ | kg $NH_3$ | kmol $NH_3$ | kmol $H_2O$ | kg $H_2O$ |

$CH_4$:

| | | | | | | |
|---|---|---|---|---|---|---|
| 1 | 1000 | 1 | 2.5 | 16.042 | 1 | 2.35 |
| | 1 | 17.031 | 1 | 1 | 1000 | t $CH_4$ |

| | | | | | |
|---|---|---|---|---|---|
| t $NH_3$ | kg $NH_3$ | kmol $NH_3$ | kmol $CH_4$ | kg $CH_4$ | t $CH_4$ |

Mass Outputs

$NH_3$ (Basis):

| | | |
|---|---|---|
| Basis | = | 1 |
| | | t $NH_3$ |

CO:

| | | | | | | |
|---|---|---|---|---|---|---|
| 1 | 1000 | 1 | 2.5 | 28.014 | 1 | 4.11 |
| | 1 | 17.031 | 1 | 1 | 1000 | t CO |

| | | | | | |
|---|---|---|---|---|---|
| t $NH_3$ | kg $NH_3$ | kmol $NH_3$ | kmol CO | kg CO | t CO |
| | t $NH_3$ | kg $NH_3$ | kmol $NH_3$ | kmol CO | kg CO |

$H_2$:

| | | | | | | |
|---|---|---|---|---|---|---|
| 1 | 1000 | 1 | 6 | 2.016 | 1 | 0.71 |
| | 1 | 17.031 | 1 | 1 | 1000 | t $H_2$ |

| | | | | | |
|---|---|---|---|---|---|
| t $NH_3$ | kg $NH_3$ | kmol $NH_3$ | kmol $H_2$ | kg $H_2$ | t $H_2$ |

**A. 3: Theoretical mass inputs and outputs necessary for the corresponding energy audit in A. 1, based on eqs 1-4 in A. 2.**

| Chemical Energy Inputs (LHV) | | | | |
|---|---|---|---|---|
| LHV - $CH_4$: | | | | |
| 8.026E+08 | 1 | 1000 | 1 | 50.03 |
| 1 | 16.043 | 1 | 1.00E+09 | GJ $t^{-1}$ |
| | | | | |
| J | kmol | kg | GJ | |
| kmol | kg | t | J | |

| Chemical Energy Outputs (LHV) | | | | |
|---|---|---|---|---|
| LHV - $NH_3$: | | | | |
| 3.168E+08 | 1 | 1000 | 1 | 18.60 |
| 1 | 17.031 | 1 | 1.00E+09 | GJ $t^{-1}$ |
| | | | | |
| J | kmol | kg | GJ | |
| kmol | kg | t | J | |
| | | | | |
| LHV - $H_2$: | | | | |
| 2.418E+08 | 1 | 1000 | 1 | 119.94 |
| 1 | 2.016 | 1 | 1.00E+09 | GJ $t^{-1}$ |
| | | | | |
| J | kmol | kg | GJ | |
| kmol | kg | t | J | |
| | | | | |
| LHV - CO: | | | | |
| 2.830E+08 | 1 | 1000 | 1 | 10.10 |
| 1 | 28.01 | 1 | 1.00E+09 | GJ $t^{-1}$ |
| | | | | |
| J | kmol | kg | GJ | |
| kmol | kg | t | J | |

**A. 4: Converted chemical energy inputs and outputs based on lower heating values from the literature for the energy audit in A. 1.**

# Appendix B - Applied Thermodynamics: A Review

Probably the first time anyone paid attention to the potential of thermodynamics was when Haber studied the equilibrium between ammonia and its elements in eq (1).[71] Classical (macroscopic) thermodynamics can be loosely defined as the study of equilibrium and heat transfer between phases.[71] Equilibrium denotes not only the absence of macroscopic change but also the absence of any tendency toward macroscopic change. No change in state can occur in a system at equilibrium. Furthermore as a driving force results in a tendency towards change, the absence of such a tendency indicates an absence of any driving force acting on the system.[96] A phase is defined phenomenologically to be a physically and chemically homogenous substance irrespective of amount and shape. Each phase has a limited region of existence concerning temperature, pressure, and composition.[86] Thermodynamics addresses what is theoretically possible at given conditions and answers why any change in the system occurs at all.[28]

## A.1 Gibbs Free Energy Minimization

The *Gibbs free energy*, $\Delta G$, is a characteristic thermodynamic function. That is, all thermodynamic functions for the reaction can be expressed in terms of the Gibbs energy and its derivative with respect to its independent variables (temperature, pressure, and composition). Simply stated, the Gibbs free energy completely defines the thermodynamic behavior of the system without the need of other thermodynamic quantities. It fully defines equilibrium conditions and is a measure of useful energy available from the reaction.[28,86]

Consider the generic equilibrium chemical reaction between reactants A and B and products C and D where $n_i$ represents the number of moles of species i as shown in eq (16). For a closed system, the Gibbs free energy of the chemical reaction can be calculated via eq (17).[66]

$$n_A A + n_B B \leftrightarrow n_C C + n_D D \quad (16)$$

$$\Delta G^{rxn} = \sum_{i=prod.} n_i g_i^f - \sum_{j=react.} n_j g_j^f \quad (17)$$

Where $\Delta G^{rxn}$ is in kJ mol$^{-1}$, n are moles of product component i or reactant component j, and $g^f$ is the Gibbs energy of formation for component i or j in kJmol$^{-1}$ from tabulated data.[71,72,86] If the reaction products are thermodynamically favored at equilibrium, $\Delta G^{rxn}$ is negative and represents the maximum useful work available from the reaction. However if the reactants are thermodynamically favored at equilibrium, $\Delta G^{rxn}$ is positive and represents the minimum amount of energy that must be supplied to the system to make equilibrium favor products.

The true equilibrium constant for eq (16) is calculated by eq (18) assuming ideal gas and solid phases.[66,94]

$$K_T = exp\left[-\frac{\Delta G^{rxn}}{RT}\right] = \prod_{i=prod.} n_i^{S_i} \prod_{j=react.} n_j^{-S_j} \left(\frac{P}{n}\right)^{S_i - S_j} \quad (18)$$

Where $K_T$ is the "true" dimensionless equilibrium constant, T is absolute temperature (K), and R is the gas constant in kJ mol$^{-1}$ K$^{-1}$, P is the total pressure in MPa, $S_i$ and $S_j$ are reaction stoichiometric coefficients, and n (mol) is the total number of reactants and products at complete conversion.[66]

The Gibbs free energy for any closed system can be calculated via equation (19).[86] Employment of equation (19) is most useful when a specific reaction or reaction pathway is unclear but possible chemical species are fairly easy identify and their molar Gibbs energies have been empirically determined and previously tabulated. The mathematical expression for the equilibrium requirement as specified by the Gibbs energy is shown in equation (20).[86]

$$\Delta G^{sys}_{T,P=const.} = \sum_i n_i g_i^f \quad (19)$$

$$\Delta G^{Equil.}_{T,P=const.} = minimum \quad (20)$$

Equations (19) and (20) can be combined, together with literature data for molar Gibbs energy of formation, to allow thermodynamic analysis to be performed on any closed system

requiring only that the temperature, pressure, and initial composition of the system be specified along with all possible chemical species.[86] Furthermore, equations (16) - (19) can be combined with equation (20) in a computational thermodynamic simulation to minimize the Gibbs free energy for a reaction or for a system while varying temperatures, pressures, or initial compositions of the system. The result reports expected products, reactant conversions, and overall system composition at equilibrium for the varied conditions.[86,96]

## A.2 Macroscopic Thermodynamics and the Open System

While the preceding thermodynamic analysis represents a good place to begin, it is important to note that it applies to closed systems only. That is, this type of analysis does not apply in open flow systems such as those considered in Figure 2.3 or Figure 3.2. Macroscopic thermodynamic analyses are a good place to start however when considering chemical equilibrium reactions in open systems (and has been used as such in the literature).[59,66] A chemical reaction is considered to be "spontaneous" when $\Delta G^{rxn} \leq 0$.[28] That is, an energetic driving force exists which is pushing the reaction toward the products. In this case, $K_T \geq 1$ from eq (18). However, if $\Delta G^{rxn} > 0$, then the driving force is lacking and $K_T < 1$. Depending on the thermochemistry of the system, $K_T < 1$ may not necessarily spell disaster in open systems where

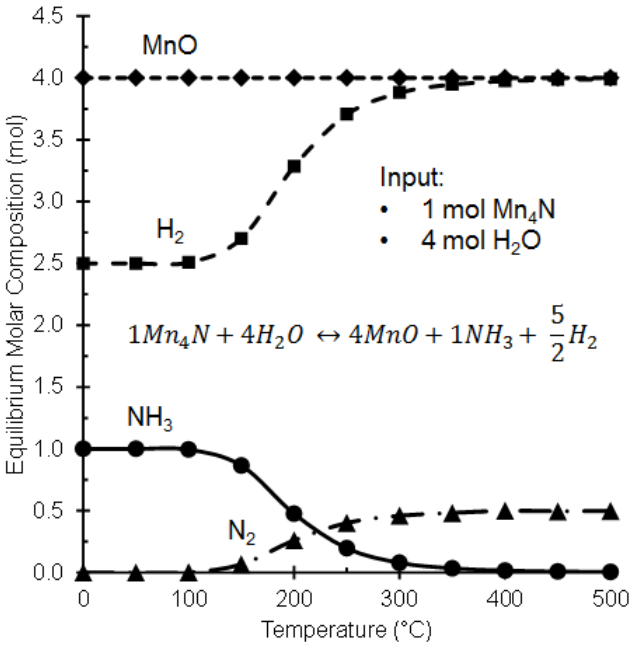


**B. 1: Equilibrium molar composition of the nitride corrosion system where $NH_3$ decomposition products are thermodynamically favored above 300 °C.**

mass is exchanged with the surroundings. A closed system will reach equilibrium and resist change in temperature, pressure, and composition. However constantly purging a product will shift equilibrium more toward the products according to Le Chatelier's principle.[28]

Figure B. 1 shows the equilibrium molar compositions of the $Mn_4N$ corrosion reaction,[90] similar to eq (6), where $NH_3$ is thermodynamically unstable above 300 °C, yet temperatures of 500 °C are kinetically necessary. Employment of an open system (Figure 2.3) remedies this by removing the desired $NH_3$ product and cooling it before it can decompose into $N_2$ and $H_2$. In this fashion one can achieve the improved reaction rate observed at higher temperatures without losing the desired product.

# Appendix C - Experimental Elements of Powder X-Ray Diffraction

Powder x-ray diffraction (XRD) is a robust and convenient technique for quantitative analysis of solid samples. In principle, XRD exploits constructive interference of x-rays after they have been diffracted from electrons in a solid sample.[97] The diffraction pattern generated (see Figure 3.8 for an example) functions as an empirical "finger-print" corresponding to a specific crystal structure which can be referenced back to a database such as the International Centre for Diffraction Data[78] (ICDD) PDF-2 for both qualitative and quantitative phase identification. Phase quantification is challenged due to the loss of information in the transition from a diffraction pattern (Debye-ring) to the projected powder diffraction intensity.[97] Regardless, XRD analysis is beneficial as it does not destroy the sample and sample preparation is fast and relatively painless. The work presented herein relied on (and perhaps overused) XRD significantly due to its convenience. However an additional or parallel method for phase quantification should be considered for further experimentation.

Relevant to this work is the quantification of nitrogen within the solid lattice either after a nitridation experiment, in which the lattice should gain nitrogen, or after an $NH_3$ synthesis reaction, in which the lattice should lose nitrogen. When analyzing a solid sample possessing more than 2 phases, one should make note of the following concerns.

## C.1 The Reference Intensity Ratio

The reference intensity ratio method[98] for quantitative phase identification is so ubiquitous the $I/I_c$ ratios are now published on many entries of the PDF[78]. Intensities of peaks of interest in a sample of known phases but unknown composition (wt.%) are compared with the intensities of peaks for pure corundum, hence $I/I_c$. In theory, this allows for quick and easy calculation of phase compositions within a sample. Unfortunately *published* $I/I_c$ ratios lack the necessary accuracy due

to a variety of errors including inhomogeneous samples preparation, preferred orientations, and variable crystallinity.[99] Yet the ubiquity of this method makes getting a number, even if it is the wrong number very, very easy. To achieve an accurate phase composition, a method involving an internal or external standard or Rietveld refinement should be employed.[99]

## C.2 X-Ray Penetration Depth

The depth of penetration, t, of x-rays into a sample is described by eq (21):[100]

$$t = \frac{3.45 \sin \omega}{\frac{\mu}{\rho}\rho_{bulk}} \quad (21)$$

Where ω is the angle of incidence, μ/ρ is the mass absorption coefficient, and $\rho_{bulk}$ is the density and packing factor of the sample. The wavelength of radiation also plays an important role. For Cu-Kα radiation and tungsten with a 60% packing factor, t is only 4 μm. As such the particle size would need to be sufficiently less than 4 μm in order to "see" into the particle.

## C.3 Quantifying Nitrogen

Since XRD only provides a semi-quantitative approach for solid sample analysis of particle sizes ≥ 10 μm without Rietveld refinement or a method involving a standard, parallel means of quantifying lattice nitrogen are encouraged. An attractive option is elemental (or CHNS/O) analysis typically used for biological or fuel-type materials. However examples exist in the literature of success with this method.[101] The present work has also successfully used the Perkin Elmer 2400 Series II Elemental Analyzer however, these results are not shown. Other options include Energy-dispersive x-ray spectroscopy (EDX) or Kjeldahl's method.